State-wide California 2020 Carbon Dioxide Budget Estimated with OCO-2 and OCO-3 satellite data

Matthew S. Johnson[1*], Sofia D. Hamilton[2], Seongeun Jeong[2], Yu ~~yan~~ Yan Cui[3], Dien Wu[4], Alex Turner[5], Marc Fischer[2]

[1]Earth Science Division, NASA Ames Research Center, Moffett Field, CA, USA
[2]Energy Analysis and Environmental Impacts Division, Lawrence Berkeley National Laboratory, Berkeley, CA, USA
[3]Independent Researcher, Sacramento, CA, USA.
[4]Division of Geological and Planetary Sciences, California Institute of Technology, Pasadena, CA, USA
[5]Department of Atmospheric Sciences, University of Washington, Seattle, WA, USA

[*]Correspondence: Matthew S. Johnson (matthew.s.johnson@nasa.gov)

Abstract

Satellite observations are instrumental in observing spatiotemporal variability in carbon dioxide (CO_2) concentrations which can be used to derive fluxes of this greenhouse gas. This study leverages NASA's Orbiting Carbon Observatory-2 and -3 (OCO-2/3) CO_2 observations with a Gaussian Process (GP) machine learning inverse model, a Bayesian non-parametric approach well-suited for integrating the unique spatiotemporal characteristics of these satellite observations, to estimate sub-regional CO_2 fluxes. Utilizing the GEOS-Chem chemical transport model (CTM) which simulates column-average CO_2 concentrations (XCO_2) for 2020 in California – a period marked by the Coronavirus disease (COVID-19) pandemic, drought conditions, and significant wildfire activity – we estimated state-wide CO_2 emission rates constrained by OCO-2/3. This study developed prior fossil fuel emissions to reflect reduced activities during the COVID-19 pandemic, while net ecosystem exchange (NEE) and fire emissions were derived based on satellite data. GEOS-Chem source-specific XCO_2~~XCO2~~ concentrations for fossil fuels, NEE, fire, and oceanic sources were simulated coincident to OCO-2/3 XCO_2~~XCO2~~ retrievals to estimate state-wide sector-specific and total CO_2 emissions. GP inverse model results suggest annual posterior median fossil fuel emissions were consistent with prior estimates (317.8 and 338.4~~±46.4~~ Tg CO_2 yr^{-1}, respectively; 95% confidence level) and that posterior NEE fluxes had less carbon uptake compared to prior fluxes (-36.8~~±32.8~~ vs. -99.2 Tg CO_2 yr^{-1}, respectively; 95% confidence level). Posterior fire CO_2 emissions were estimated to be 68.0~~±50.6~~ Tg CO_2 yr^{-1} which was much lower compared to a priori estimates (103.3 Tg CO_2 yr^{-1}). The total median annual CO_2 emissions for the state of California in 2020 were estimated to be 349.6 Tg CO_2 yr^{-1} (range of 272.8 – 428.6 Tg CO_2 yr^{-1}; 95% confidence level), aligning closely with the prior total estimate of 342.5 Tg CO_2 yr^{-1}. This study, for the first time, demonstrates that OCO-2/3 XCO_2~~XCO2~~ observations can be assimilated into inverse models to estimate state-wide, source-specific CO_2 fluxes on a seasonal- and annual-scale.

Short Summary. Satellites, such as NASA's Orbiting Carbon Observatory-2 and -3 (OCO-2/3), retrieve carbon dioxide (CO_2) concentrations which provide vital information for estimating surface CO_2 emissions. Here we investigate the ability of OCO-2/3 retrievals to constrain CO_2 emissions for the state of California for the major emission sectors (i.e., fossil fuels, net ecosystem exchange, wildfire).

1. Introduction

Carbon dioxide (CO_2) is the most abundant greenhouse gas in Earth's atmosphere and contributes predominantly to the present-day increase in global radiative forcing (Dunn et al., 2022). Due primarily to anthropogenic emissions from fossil fuel production and usage, global concentrations of CO_2 have nearly doubled since the beginning of the pre-industrial era (Gulev et al., 2021; Lan et al., 2023). A recent comprehensive budget analysis of global CO_2 fluxes suggests that as of 2022 anthropogenic emissions are ~10 Gt C yr^{-1} (primarily from combustion of coal, oil, and natural gas) with an oceanic and terrestrial uptake offset of ~3 Gt C yr^{-1} and ~4 Gt C yr^{-1}, respectively (Friedlingstein et al., 2023). According to this report, the United States (US) contributes 14% (~1.4 Gt C yr^{-1}) of global CO_2 anthropogenic emissions. The sectors contributing the most to US anthropogenic emissions are transportation, electricity generation, and industry (EPA, 2023). One of the larger emitters of greenhouse gases in the US is the state of California which as of 2021 contributes ~0.1 Gt C yr^{-1} of CO_2 (CARB, 2023). In 2006, the state of California passed Assembly Bill 32 (AB 32) which required that by 2020 the state's greenhouse gas emissions must be reduced to 1990 levels. California was able to achieve this goal ~~but~~ and in order to ~~validate~~ demonstrate this, and the success of other future emission reduction goals, it is vital to have accurate estimates of past- and present-day greenhouse gas emissions.

Bottom-up inventories of CO_2 are commonly used to derive country-level to state-wide fossil fuel anthropogenic emissions in the US (e.g., Andres et al., 2012; CARB, 2023). Calculations of natural sources and sinks (e.g., terrestrial and marine biosphere, wildfires) contributing to total CO_2 emissions are frequently estimated using model predictions (Friedlingstein et al., 2023). The California Air Resources Board (CARB) has quantified state-wide greenhouse gas emissions for California between 2000-2021 (CARB, 2023). Anthropogenic and natural bottom-up CO_2 flux estimates are typically implemented in atmospheric transport models and compared to atmospheric observations in order to assess their accuracy. In situ observations of CO_2 from ground-based, tower, and aircraft platforms, due to their high accuracy and precision, are most frequently used to evaluate the quality of these emission estimates (Graven et al., 2018; Cui et al., 2022). While highly accurate, these types of in situ observations are limited in their spatiotemporal coverage and ability to constrain large regions and annual cycles of emissions. The assimilation of satellite-retrieved column-averaged dry-air mole fraction of CO_2 (XCO_2 ~~$XCO2$~~) (e.g., Orbiting Carbon Observatory-2 (OCO-2), Orbiting Carbon Observatory-3 (OCO-3), Greenhouse Gases Observing Satellite (GOSAT), GOSAT-2, Carbon Dioxide Monitoring constellation (CO2M), TanSat) into atmospheric transport models has been demonstrated to be able to constrain emissions on a global- to country-level scale more effectively in regions which lack dense in situ measurement networks (Pandey et al., 2016; Yang et al., 2021; Peiro et al., 2022; Philip et al., 2022; Imasu et al., 2023; Byrne et al., 2023; Noël et al., 2024). This study focuses on CO_2 fluxes in the state of California, where OCO-2 and OCO-3 have been used to constrain urban-scale emissions in the mega-city of Los Angeles (Hedelius et al., 2018; Ye et al., 2020; Kiel et al., 2021; Wu et al., 2022; Roten et al., 2023). However, to-date, no studies have demonstrated the capability to evaluate and constrain CO_2 fluxes using satellite-retrieved information on a state-wide spatial domain such as California. For California and other states this is important because some state agencies only release state-wide inventories (not specifically for urban areas) and many climate programs are generated based on the state-wide inventories.

While satellite-based atmospheric inverse modeling provides a significantly enhanced method for quantifying CO_2 emissions, using satellite observations in atmospheric inversions introduces two principal challenges. These include: 1) incorporating the spatiotemporal covariance inherent in satellite data and 2) accurately estimating the hyperparameters, such as the length scale, of this covariance. Satellite observations contain both spatial and temporal properties, which means that the data have inherent spatial and temporal characteristics that inform us about surface emissions. However, numerous inverse modeling studies have not consistently incorporated both covariance structures (Johnson et al., 2016; Fischer et al., 2017; Cui et al., 2019; Graven et al., 2018; Nathan et al., 2018; Ye et al., 2020; Wu et al., 2022; Roten et al., 2023). While some studies have accounted for both spatial and temporal covariances, they have not determined optimal hyperparameters that align with the satellite observations (e.g., Turner et al., 2020). For example, the length scale parameter is crucial for influencing the covariance, which in turn affects the estimation of the unknown functions; in many cases, however, this parameter is not estimated explicitly for its

84 optimal value but instead prescribed. In this study, we applied an atmospheric inversion system which fully utilizes
85 the spatiotemporal properties embedded in satellite data (i.e., OCO-2 and OCO-3). This system is built based on the
86 Gaussian Process (GP) machine learning (ML) approach enabled by modern Probabilistic Programming Languages
87 (PPLs). GP is an ML technique that treats predictions as distributions rather than single points, providing a measure
88 of prediction uncertainty, which is ideal for atmospheric inverse modeling (see Sect. 2.4), because posterior
89 uncertainties are vital for providing quantitative information on the confidence level of the emissions constraint.
90 ~~Inverse~~ Inversion CO_2 models, other than analytical systems, cannot always provide posterior emission uncertainties,
91 and these estimates can be unreliable and computationally expensive to calculate (e.g., Liu et al., 2014; Bousserez et
92 al., 2015). The kernels (i.e., covariance functions) of GP models are employed to capture the intricate spatiotemporal
93 correlation structures of OCO-2/3 data. PPLs have been used in previous studies (e.g., Jeong et al., 2017, 2018), but
94 modern PPLs provide significantly improved capabilities to implement GP models. Specifically, the built-in functions
95 for GP kernels in modern PPLs enhance our ability to model the covariance structure of OCO-2/3 data.

96 This study applies inverse modeling techniques following GP/ML methods described in further detail in Sect.
97 2.4 to estimate CO_2 fluxes in California for a full year ~~in~~ of 2020 using XCO_2~~XCO2~~ observations from OCO-2 and
98 OCO-3. The year 2020 had numerous anomalous features likely impacting total CO_2 fluxes in California such as
99 reduced anthropogenic emissions caused by coronavirus disease pandemic (COVID-19) lockdown procedures (Yañez
100 et al., 2022), extreme wildfire activity (Jerret et al., 2022; Safford et al., 2022), and drought conditions (Steel et al.,
101 2022). The impact these types of events have on CO_2 fluxes are challenging to predict and difficult to replicate in
102 bottom-up emission inventories. ~~The~~ This study is structured as follows: Sect. 2 presents the forward and inverse
103 models, satellite observations, and bottom-up emission inventories; Sect. 3 discusses the results of the study, and Sect.
104 4 contains the discussion and conclusions.

2. Methods

2.1 GEOS-Chem forward model

107 The forward model used to calculate atmospheric concentrations of CO_2 corresponding to OCO-2 and OCO-3
108 observations was the GEOS-Chem (version 14.0.1) chemical transport model (CTM) (Bey et al., 2001; Nassar et al.,
109 2010). GEOS-Chem was used to simulate XCO_2~~XCO2~~ concentrations corresponding to each OCO-2 and OCO-3
110 retrieval for a nested North America domain (10°–70°N, 40°–140°W) driven by Modern-Era Retrospective Analysis
111 for Research and Applications, Version 2 (MERRA-2) meteorology at $0.5° \times 0.625°$ spatial resolution using 47 vertical
112 levels from the surface to 0.01 mb. Chemical boundary conditions (BCs) of CO_2 used in the nested simulations were
113 provided by global GEOS-Chem-based 4D-Var data assimilation system runs at $4.0° \times 5.0°$ horizontal spatial
114 resolution using 47 vertical levels. These global simulations of CO_2 for the year 2020 were constrained using inverse
115 model methods through the assimilation of OCO-2 XCO_2~~XCO2~~ land nadir + land glint (LN+LG) retrievals and global
116 in situ observations (Philip et al., 2019, 2022). The bottom-up emission inventories for CO_2 fluxes from fossil fuel
117 (FF), net ecosystem exchange (NEE), wildfires, and oceans are described in Sect. 2.2. GEOS-Chem was initialized
118 with chemical BCs and run for the entire year of 2020 with two months of spin up time.

119 Total atmospheric CO_2 and source-apportioned (i.e., FF, NEE, fire, ocean, and boundary conditions)
120 concentrations were calculated over California for all OCO-2 and OCO-3 observations. These source-attributed
121 concentrations were calculated with sensitivity simulations by turning off individual source fluxes or boundary
122 conditions and comparing these results to the total atmospheric CO_2 concentration predictions from simulations with
123 all sources included. Model-simulated XCO_2~~XCO2~~ corresponding to each OCO-2 and OCO-3 retrieval (H) were
124 derived through the convolution of model CO_2 profiles with the column averaging kernel vector ($\boldsymbol{a}$) from OCO-2 and
125 OCO-3 following Eq. (1):

126
$$H = XCO2_a + \boldsymbol{a}^T(\boldsymbol{f}(\sigma(x)) - \boldsymbol{c}_a) \tag{1}$$

127 where prior profiles of CO_2 (c_a) and prior column CO_2 ($XCO2_a$) represent prior information used in the OCO-2 and

128 OCO-3 $\underline{XCO_2}$ ~~XCO2~~ retrieval (O'Dell et al., 2012) and $f(\sigma(x))$ is the GEOS-Chem-predicted vertical profiles of CO_2

129 interpolated to the retrieval levels of OCO-2 and OCO-3.

2.2 Bottom-up emission inventories

131 Bottom-up emission inventories used to drive GEOS-Chem simulations are described in Table 1 and ~~annually~~

132 ~~averaged emission rates are displayed in Fig. 1 (maps of~~ seasonally-averaged ~~emissions~~ emission maps are displayed

133 in Fig. S1~~)~~. The Vulcan version 3.0 FF emission inventory covers all anthropogenic source sectors of CO_2 in California

134 (i.e., residential, commercial, industrial, electricity production, onroad, nonroad, commercial marine vessel, airport,

135 rail, and cement) between 2010-2015 (Gurney et al., 2020). To create a spatially and temporally resolved Vulcan

136 inventory in California for the year 2020 ($V2020_M$ ~~V^M_{2020}~~), the hourly 2015 Vulcan emissions ($V2015_M$ ~~V^M_{2015}~~) are

137 scaled by an annual and a monthly scaling factor ~~(V_{2020})~~ using Eq. (2). The sector-specific annual scaling factor

138 ($R^{CARB}_{2020/2015}$) is calculated as the ratio of annual emissions~~,~~ from that sector ~~the~~ in the CARB inventory for 2020

139 ~~(C_{2020})~~ (which accounts for COVID-19 lockdown emissions reductions; CARB, 2022) to the 2015 emissions. The

140 sector-specific monthly scaling factor (R_M ~~R^M~~)~~.~~ was ~~used to calculate monthly scaling factors for each month M~~

141 ~~(R^{Month}) for CO_2 emissions in 2020 compared to 2015 (C_{2015})~~calculated from activity data from each sector, as the

142 ratio of monthly activity to annual average activity, and used to appropriately distribute reductions due to

143 ~~lockdowns~~the COVID-10 lockdown throughout the year.

144 $\qquad V2020_M$ ~~V^M_{2020}~~ $= V2015_M$ ~~V^M_{2015}~~ $\times R^{CARB}$ ~~C~~$_{2020/2015} \times R_M$ ~~R^{Month}~~

145 (2)

146 The Vulcan inventory for 2015 was then multiplied by these scaling factors to produce $V2020_M$ ~~V_{2020}~~. Both Vulcan

147 and CARB provide the same sector-level emissions estimates, so the scaling was done for each emission sector

148 separately. The scaled 2020 Vulcan inventory was then aggregated to 0.1° × 0.1° latitude and longitude.
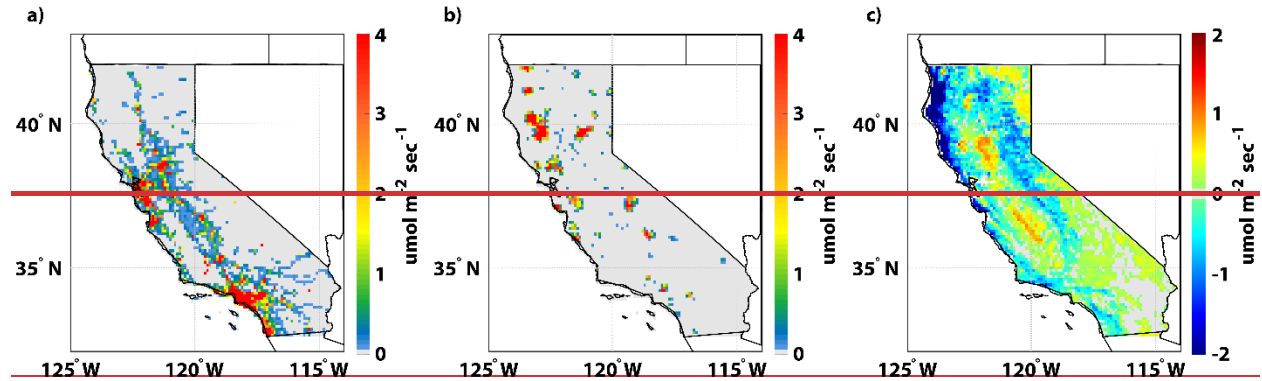
150 ~~**Figure 1. Annually-averaged 2020 CO_2 emissions (μmol m^{-2} sec^{-1}) for the state of California. Emissions from**~~

151 ~~**the terrestrial portion of the domain are shown for a) FF, b) Fire, and c) NEE.**~~

152 Natural CO_2 emission source (NEE, wildfire, and ocean) estimates were available for the year 2020 and no

153 scaling was necessary. Biospheric fluxes of CO_2 were derived using monthly 5 km × 5 km NEE calculations from the

154 Solar-Induced Fluorescence for Modeling Urban biogenic Fluxes version 1 (SMUrF v1; Wu~~e~~ et al., 2021) model.

155 SMUrF calculates gross primary production (GPP), respiration (R_{eco}), and NEE (= R_{eco} – GPP) fluxes using 1) land

156 cover type 500 m MODerate resolution Imaging Spectroradiometer (MODIS) data, 2) solar induced florescence (SIF)

157 from the OCO-2 sensor, 3) above ground biomass at 100 m resolution from GlobBiomass, 4) observed flux

158 measurements from eddy-covariance towers, and 5) gridded soil and air temperature data products. Wildfire CO_2

159 emissions were implemented using a modified Global Fire Emissions Database version 4 (GFED4) data set (van Wees

160 et al., 2022). This modified version of GFED4 was produced using MODIS burned area and fire detections data with

161 a spatial resolution of 500 m. Finally, oceanic CO_2 fluxes were derived from CarbonTracker (CT2022; Jacobson et

162 al., 2023) 1° × 1° output. These CT2022 coarse spatial scale fluxes were interpolated to match the GEOS-Chem model
163 spatial resolution.

Table 1. Bottom-up prior CO_2 emission inventories and 2020 carbon budget (Tg CO_2 yr^{-1}) for California.

Source	Inventory Name	Spatial Res.	Annual Flux: California	Reference
FF	Vulcan	1 km × 1 km	338.4	Gurney et al., 2020
NEE	SMUrF	5 km × 5 km	-99.2	Wu et al., 2021
Fire	GFED (modified)	500 m × 500 m	103.3	van Wees et al., 2022
Ocean	CarbonTracker (CT2022)	100 km × 100 km	N/A	Jacobson et al., 2023
Net			342.~~3~~5	

2.3 OCO-2 and OCO-3 observations

166 NASA has two operational satellites with the spatial resolution and precision necessary to constrain point-source to
167 regional- and global-scale CO_2 emissions (i.e., OCO-2 and OCO-3). OCO-2 was launched in 2014 and is a sun-
168 synchronous polar orbiting satellite which is in the Afternoon Constellation (A-train) of Earth Observing Satellites
169 with a local overpass time of ~1:30 pm retrieving XCO_2~~XCO2~~ at 1.3 km × 2.3 km spatial resolution (Crisp et al.,
170 2017). OCO-3 has been onboard the International Space Station (ISS) since 2019 and has an orbital inclination of
171 51.6° providing observations at varying times of the day (Eldering et al., 2019). OCO-3 makes orbital observations;
172 however, differs from OCO-2 as it has the capability to make snapshot area maps (SAMs) which cover 80 km × 80
173 km at the native spatial resolution of 1.6 km × 2.2 km. The XCO_2~~XCO2~~ retrieval~~s~~ from OCO-2 and OCO-3 both use
174 the Atmospheric Carbon Observations from Space (ACOS) algorithm (O'Dell et al., 2018) and this study applied
175 version 11r and version 10.4r of OCO-2 and OCO-3, respectively. Retrievals of XCO_2~~XCO2~~ from LN+LG retrievals
176 modes were used to compare to GEOS-Chem and estimate posterior state-wide CO_2 emissions. Since individual high
177 spatiotemporal OCO-2 and OCO-3 retrievals do not provide independent pieces of information, in this study they are
178 averaged to the 0.5° × 0.625° spatial resolution of GEOS-Chem. In total, 1614 co-located model-satellite data points
179 were available during 2020 to evaluate prior XCO_2~~XCO2~~ predictions and constrain~~ing~~ posterior CO_2 emissions. The
180 seasonal distribution (meteorological seasons: winter [December, January, February; DJF], spring [March, April,
181 May; MAM], summer [June, July, August; JJA], fall [September, October, November; SON],) of these co-locations
182 were: 386, 299, 551, and 378 for winter, spring, summer, and fall months, respectively. The spatial distribution of the
183 observational coverage provided by OCO-2+OCO-3 during 2020 is displayed in Fig. S2.

2.4 Inverse model technique

185 The inverse model developed for this study used a GP/ML framework. GP is a flexible, non-parametric approach,
186 distinguished by its use of hyperparameters, which defines a prior probability distribution over functions (Williams
187 and Rasmussen, 2006; Biship, 2007; Murphy, 2022). A GP is fully characterized by its mean function $m(\mathbf{x})$ and kernel
188 $k(\mathbf{x}, \mathbf{x}')$:

189 $$f(\mathbf{x}) \sim GP\left(m(\mathbf{x}), k(\mathbf{x}, \mathbf{x}')\right) \tag{3}$$

190 $$\mathbf{y} = f(\mathbf{x}) + \epsilon \tag{4}$$

191 where $\mathbf{y}$ is the OCO-2 and OCO-3 satellite observation vector, including additive noise ϵ (i.e., noisy version of $f(\mathbf{x})$).
192 The noise term (ϵ) is modeled as $\epsilon \sim N(0, \sigma_{noise}^2 \mathbf{I})$, where $\mathbf{I}$ is the identity matrix and σ_{noise}^2 is the noise variance
193 hyperparameter. As described in Text S3, σ_{noise} is assigned a Half-Cauchy prior distribution, and its posterior is
194 inferred using the No-U-Turn Sampler (NUTS) sampler (Hoffman and Gelman, 2014). Although sampling every
195 possible value of the function $f(\mathbf{x})$ across a continuous domain is supported, we sample a finite set of points (i.e.,
196 OCO-2/3 observation time and locations), leading to a vector of function values, $\mathbf{f} = [f(\mathbf{x}_1), f(\mathbf{x}_2), ..., f(\mathbf{x}_N)]$,

197 which follows a joint Gaussian distribution with mean vector $\boldsymbol{\mu} = m(\mathbf{x}_1), m(\mathbf{x}_2), \dots, m(\mathbf{x}_N)$ and covariance matrix
198 $[Cov]_{i,j} = k(\mathbf{x}_i, \mathbf{x}_j)$. In this work, the terms "kernel" and "covariance function" are used synonymously.

199   For our flux inference application, we define the mean function $m(\mathbf{x})$ as:

200       $m(\mathbf{x}) = \boldsymbol{K}\boldsymbol{\lambda} + \mathbf{D}$ (5)

201 where $\boldsymbol{K}$ is the input data, a $n \times k$ matrix, derived from GEOS-Chem model predictions, $\boldsymbol{\lambda}$ is a vector ($k \times 1$) of
202 scaling factors, which quantify the adjustment required for our prior emissions estimates to be consistent with
203 observations, and $\mathbf{D}$ is the systematic bias. In this work, we estimate a single value for $\mathbf{D}$ for each month in 2020.
204 Thus, each element of vector $\mathbf{D}$ is populated with the same value for each month of 2020. We assume that this bias
205 term captures systematic bias due to instrument error, model transport error, and GEOS-Chem BC errors (Jeong et al.,
206 2017). We show the probability density function of the estimated bias hyperparameter by month in Fig. S3. The
207 median values range from –0.99 to 0.71 ppm, depending on the month. As noted, this value reflects the combined bias
208 arising from atmospheric transport, boundary conditions, or other potential sources of error. This approach to
209 addressing model bias has been applied in previous studies (e.g., Jeong et al., 2017). In this work, we included the
210 bias term in the mean function [Eq. (5)]. As in Jeong et al. (2017), we model the bias term ($\mathbf{D}$) as a single component
211 in the GP mean function due to the lack of prior information needed to separate it into identifiable sources (e.g.,
212 transport or boundary condition errors). Introducing multiple terms without such constraints would risk overfitting
213 and model instability. Here, $\mathbf{D}$ and $\boldsymbol{\lambda}$ are considered a GP hyperparameter because it directly scales $m(\mathbf{x})$. This mean
214 function has been widely adopted in atmospheric inverse analysis for estimating greenhouse gas emissions (Jeong et
215 al., 2017; Ye et al., 2020; Ohyama et al., 2023). In GP modeling, it is important to note that the function $\mathbf{K}\boldsymbol{\lambda} + \mathbf{D}$ is
216 used as the mean of the latent (i.e., unknown) GP function, $f(\mathbf{x})$. In traditional Bayesian inversion methods (e.g.,
217 Jeong et al., 2017), the mean function ~~was~~ are directly related to $\mathbf{y}$ in the form $\mathbf{y} = \mathbf{K}\boldsymbol{\lambda} + \mathbf{D} + \epsilon$. The prior distributions
218 for $\boldsymbol{\lambda}$ and other hyperparameters are described in Text S3.

219   The second component of a GP is the covariance function (i.e., GP kernel), which dictates how function
220 values at different points relate. For the spatial part of the kernel, we employ the Matérn 5/2 kernel, a widely used
221 covariance function for modeling spatial data (Bevilacqua et al., 2022). The Matérn 5/2 kernel between two spatial
222 points can be expressed as:

223       $k(\mathrm{x}, \mathrm{x}') = \left(1 + \frac{\sqrt{5}r}{\ell_s} + \frac{5r^2}{3\ell_s^2}\right) \exp\left(-\frac{\sqrt{5}r}{\ell_s}\right)$ (6)
224       $r = \sqrt{(x_1 - x'_1)^2 + (x_2 - x'_2)^2}$ (7)

225 where r is the Euclidean distance between the points x and x', x_1 and x_2 represent longitude and latitude, and ℓ_s is
226 the spatial length scale. The length scale is typically prescribed, estimated, or computed based on independent data
227 (Baker et al., 2022). In this work, we estimate it simultaneously with other hyperparameters (e.g., the scaling factors).
228 We used the Squared Exponential kernel for the temporal covariance to express the relationship between two temporal
229 points:

230       $k_\mathrm{t}(\mathrm{x}, \mathrm{x}') = \exp\left(-\frac{(x_3 - x'_3)^2}{2\ell_t^2}\right)$ (8)

231 where x_3 denotes the time and ℓ_t is the temporal length scale. The spatiotemporal kernel matrix is then constructed
232 by multiplying the spatial and temporal kernels:

233       $k_\mathrm{st}(\mathbf{x}, \mathbf{x}') = \sigma^2 k_\mathrm{s}(\mathbf{x}, \mathbf{x}') \cdot k_\mathrm{t}(\mathbf{x}, \mathbf{x}')$ (9)

234 where σ^2 denotes the variance of the kernel, which scales the amplitude of the function values predicted by the GP.
235 The spatiotemporal kernel, k_st, is realized by element-wise multiplication of the spatial, k_s, and temporal, k_t, kernels.
236 The resulting spatiotemporal kernel maintains the dimensionality of its constituent kernels.

237   We perform inversions using three distinct mean functions as depicted in Eq. (5). Model 1 incorporates a
238 systematic bias term **D**, assuming a normal distribution with a mean of 0 and a standard deviation (sd) of 0.5 ppm.
239 Model 2 resembles Model 1 but adopts a standard deviation of 1.0 ppm for the bias term. In contrast, Model 3 excludes
240 the systematic bias term **D** and instead corrects the OCO-2 or OCO-3 a priori and background concentrations by
241 applying scaling factors, thus addressing any biases in the OCO-2 or OCO-3 a priori and background concentrations
242 multiplicatively. We evaluate the three GP models using their expected log pointwise predictive density (ELPD), a
243 metric for model predictive performance. Further details on the model comparison through ELPD are provided in the
244 Supporting Information (Text S1 and ~~Figure~~ Fig. ~~S2~~S4).

245   We employed the Markov chain Monte Carlo (MCMC) method to estimate the hyperparameters of the GP
246 model framework. MCMC has been utilized in several atmospheric inverse modeling studies (Ganesan et al., 2014,
247 2015; Jeong et al., 2016, 2017, 2018). However, we adopt the ~~No-U-Turn Sampler (~~NUTS~~)~~, a modern and advanced
248 MCMC algorithm (Hoffman and Gelman, 2014). We utilized the PyMC PPL (Abril-Pla et al., 2023) to implement the
249 NUTS algorithm for MCMC sampling, generating 4,000 samples each month following a tuning phase of 3,000 steps.
250 More details for the GP model structure and the prior distribution for the hyperparameters are described in the
251 ~~Supporting Information~~ Text S2. Using the prior distributions specified in Text S3, we inferred the posterior
252 distributions of the GP hyperparameters using the NUTS algorithm, implemented via the PyMC framework. In our
253 approach, all hyperparameters are estimated jointly. That is, the scaling factors are estimated simultaneously with
254 other parameters, such as the kernel length scales (Jeong et al., 2025). This method enables full posterior inference of
255 the hyperparameters, offering a more robust characterization of uncertainty than point estimation methods. More
256 details on hyperparameter optimization for the GP model are provided in Jeong et al. (2025).

257   ~~We employed the Markov chain Monte Carlo (MCMC) method to estimate the hyperparameters of the GP~~
258 ~~model framework. MCMC has been utilized in several atmospheric inverse modeling studies (Ganesan et al., 2014,~~
259 ~~2015; Jeong et al., 2016, 2017, 2018). However, we adopt the No-U-Turn Sampler (NUTS), a modern and advanced~~
260 ~~MCMC algorithm (Hoffman and Gelman, 2014). We utilized the PyMC PPL (Abril-Pla et al., 2023) to implement the~~
261 ~~NUTS algorithm for MCMC sampling, generating 4,000 samples each month following a tuning phase of 3,000 steps.~~
262 ~~More details for the GP model structure and the prior distribution for the hyperparameters are described in the~~
263 ~~Supporting Information Text S2 and Figure S3.~~

2.5 Evaluation techniques

265 Prior and posterior emissions can be indirectly evaluated using atmospheric observations for accuracy and uncertainty
266 ~~using~~ applying normalized mean bias (NMB) and root mean square error (RMSE), respectively (Vermote and
267 Kotchenova, 2008). GEOS-Chem forward and inverse model simulations were evaluated using daily OCO-2 and
268 OCO-3 LN+LG XCO_2~~XCO2~~ retrievals during 2020. These model predictions were evaluated for each season to
269 determine the accuracy of prior and posterior emissions and BCs which have large variability throughout the year (see
270 seasonal a priori emissions in Fig. S1). General statistical parameters were used to evaluate model simulations: NMB,
271 RMSE, correlation coefficient (R), and simple ordinary least-squares linear regression (slope, y-intercept, etc.).
272 Calculations of NMB are normalized by OCO-2 and OCO-3 observation values as shown in Eq. (10):

273
$$NMB = \frac{\sum_{i=1}^{N}(M_i - y_i)}{\sum_{i=1}^{N} y_i} \tag{10}$$

274 where N is the total number of model (M_i) and OCO-2 and OCO-3 (y_i) co-locations. Equation (11) is used to calculate
275 RMSE values:

276
$$RMSE = \sqrt{\frac{\sum_{i=1}^{N}(M_i - y_i)^2}{N}} \tag{11}$$

3. Results

3.1 California prior emissions

According to prior emission inventories used in this study, the majority of CO_2 emitted in California is from anthropogenic FF sources (see Table 1). The Vulcan FF emission inventory, scaled to 2020 emissions using the CARB state-wide inventory, suggests that anthropogenic sources contributed 338.4 Tg CO_2 yr^{-1}, and these sources are primarily located in the Los Angeles Basin and San Francisco Bay Areas where there are highly populated cities (see Fig. S1). It is estimated that CO_2 emissions in 2020 were reduced by ~10% compared to 2019 due to COVID-19 restrictions (CARB, 2022). According to GFED4, a total of 103.3 Tg CO_2 yr^{-1} was emitted from biomass burning during 2020, which was one of the most active wildfire years in California on record. Figure S1 shows that the majority of these emissions came from the large wildfires which occurred in northern and central California. These fire emissions were nearly offset by the biospheric uptake of CO_2 in California of -99.2 Tg CO_2 yr^{-1} estimated by the SMUrF model (i.e., our prior model). The largest NEE uptake is estimated to occur in the forested regions of northern California and the Sierra Nevada Mountains and largest respiration fluxes were in the Sacramento and San Joaquin Valley areas and the Tulare Basin.

For emission sources other than FF, such as wildfire and NEE, CO_2 fluxes in the bottom-up data products had noticeable seasonality (see Fig. S1). Wildfires in 2020 had pronounced emissions during the summer and fall months compared to minimal emissions in the winter and spring which is California's rainy season. The fire season of 2020 was exceptionally active with multiple large complexes occurring between August and September (Keeley and Syphard, 2021). Prior emissions suggest that in California between August and September fires emitted 95.4 Tg CO_2 which was 92% of the annual total. Biospheric fluxes also displayed large seasonality with largest uptake in the warmer growing season during the spring and summer and highest respiration rates during the colder months of the winter and fall. NEE uptake peaked between May and June with average monthly uptake rates of around -27.0 Tg CO_2 while respiration peaked between September and October with average monthly rates ~11.0 Tg CO_2. Less seasonality is apparent in Vulcan 2020 FF emissions for California, with monthly emission rates ranging between 23.0 and 32.0 Tg CO_2; however, our CARB-adjusted prior FF model does capture the decrease in anthropogenic CO_2 emissions upon the initiation of the COVID-19 lockdown during spring 2020.

3.2 Evaluation of model-simulated XCO_2~~XCO2~~ using prior emissions

To indirectly evaluate a priori bottom-up emissions, GEOS-Chem forward model simulations were evaluated with OCO-2 and OCO-3 XCO_2~~XCO2~~ retrievals. Figure ~~2~~ 1 shows the comparison of modeled and satellite XCO_2~~XCO2~~ values using prior emissions and observations by season. A timeseries of daily co-located prior and posterior model predicted XCO_2 compared to OCO-2/3 observations during the year 2020 is also displayed in Fig. S6 (histogram of annual prior and posterior residuals displayed in Fig. S7). For spring months, GEOS-Chem using prior emissions displayed a slight high bias (NMB=1.1 ppm) and low correlation (R = 0.38) as the model did not capture the variability of XCO_2~~XCO2~~ retrieved by satellites. While the model captures the mean XCO_2~~XCO2~~ values observed, high and low values observed in the spring months were not replicated by the model (linear regression slope = 0.24). A similar evaluation was derived for the winter months as the model had a similar high bias (NMB=1.0 ppm), low correlation (R = 0.39), and relatively low linear regression slope (0.24). A somewhat different comparison was calculated between the model with prior emissions and observations for the summer and fall months. The GEOS-Chem simulations during the summer were able to capture the variability in satellite-retrieved XCO_2~~XCO2~~ values with high correlation (R = 0.73) and linear regression slope of 0.75. The model and prior emissions resulted in a small negative bias during the summer months (NMB=-0.4 ppm). The prior model runs had the least bias in the fall months (NMB=-0.3 ppm) and also displayed moderate correlation (R = 0.52) and linear regression slope (0.34). The evaluation of the prior model displayed similar RMSE values throughout 2020 ranging between 1.4 and 1.8 ppm with the largest random error in the fall months and lowest values in the summer. GEOS-Chem using prior emission displayed biases and errors which varied by season and suggests that observational constraint could improve the estimates of CO_2 emission in California. The following sections present the inversion of CO_2 emissions when assimilating satellite-derived XCO_2~~XCO2~~ values and the evaluation of posterior emissions.

324
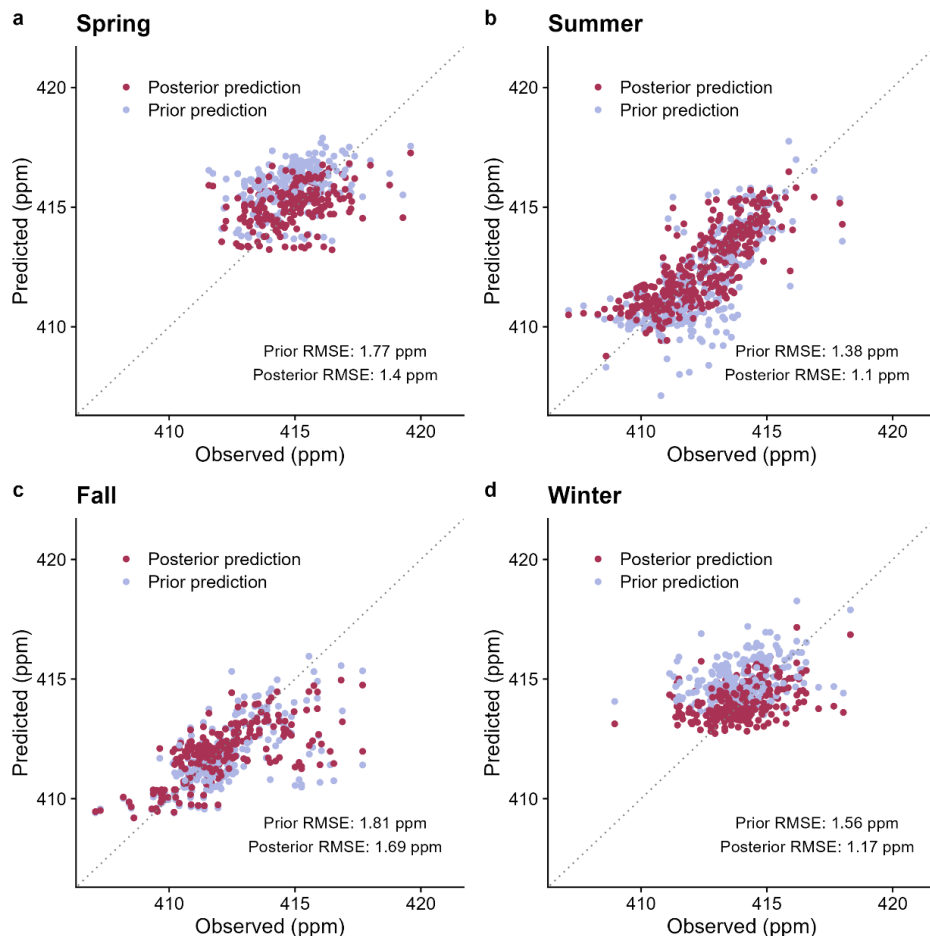
Figure 21. Comparison of seasonal GEOS-Chem XCO₂XCO2 predictions (ppm) using prior (blue) and posterior (purple) emissions and observed OCO-2 and OCO-3 concentrations (ppm). This result is based on the GP inversion model with a systematic bias of 0.5 ppm (Model 1). RMSE values for the prior and posterior model simulations are presented in the figure legend.

3.3 Inverse GP model evaluation

This section describes the evaluation of the GP inversion model using posterior predictive checks (PPCs). PPCs ensure that the inversion results accurately represent the observed data (Gelman et al., 1996). The method involves using the posterior distribution of the model parameters to generate new datasets, which are then compared to the actual observed data. PPCs assess whether the model is capable of producing data similar to the observed data, thereby providing insight into the model's ability to capture the data-generating process accurately. Text S1 describes the comparison of the different GP inversion model setups and how Model 1 performs most accurately. Due to the best performance by Model 1, the rest of the results in this study are based on these outputs. Figure 3 2 shows PPCs using probability density functions (PDFs) for the middle of each season (except January) using Model 1. Due to an insufficient number of OCO-2 and OCO-3 XCO₂XCO2 observations (N < 10) in January, the PPC for February is included instead to represent the winter season. We construct the PDFs by utilizing local enhancements in XCO₂XCO2 concentrations after subtracting the OCO-2 or OCO-3 a priori XCO₂XCO2 and modeled BCs from the total satellite XCO₂XCO2 concentrations. The results in Fig. 3 2 demonstrate that the data generated from the Model 1 posterior parameters generally agree with observations.

343
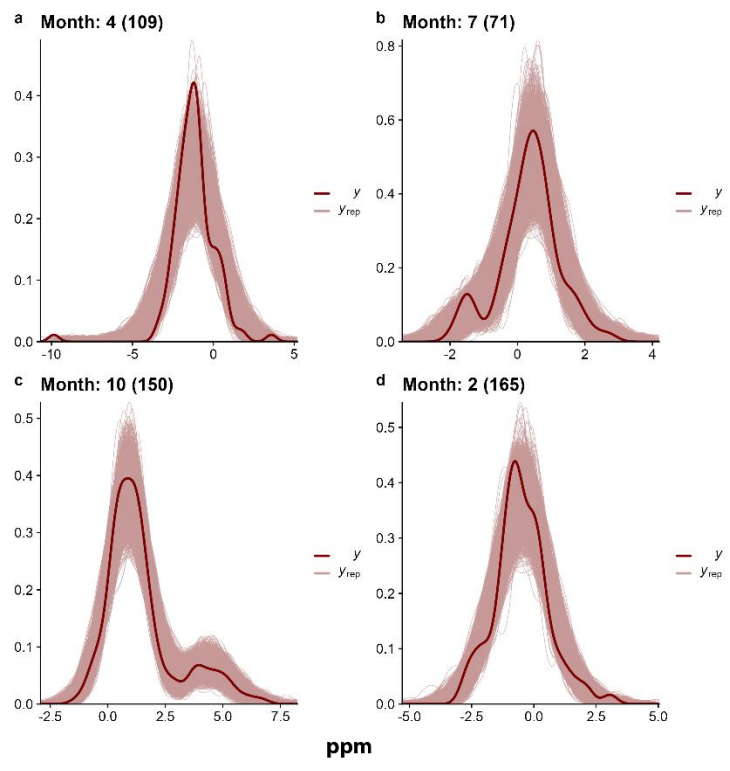
Figure 3̶2. Evaluation of the GP inverse model (Model 1) performance using PPCs for months representative of each season in 2020 (April = spring; July = summer; October = fall; February = winter). The observed satellite XCO_2X̶C̶O̶2̶ data (y; in units of ppm) are represented by the bold lines, while the fine lines (y_{rep}) depict 4000 samples (in units of ppm) simulated with parameters drawn from the posterior distributions. Each sample (i.e., each fine line) for each month is of equivalent size to the number of the model-observation co-locations (noted in parentheses).

The comparison between the posterior predictions from the GP inversion and the observed satellite XCO_2X̶C̶O̶2̶ data indicates an improvement in the RMSE for all seasons (posterior RMSE values on average ~17% lower compared to prior model simulations), suggesting a more accurate model fit than the initial prior predictions (see Fig. 1F̶i̶g̶u̶r̶e̶ ̶2̶). The GP inversion was also able to remove the majority of systematic bias imposed by the prior emissions a̶l̶o̶n̶g̶ ̶w̶i̶t̶hand BCs used in the nested GEOS-Chem simulations along with improving correlation with satellite XCO_2X̶C̶O̶2̶ observations. For spring months, posterior model simulations displayed a small bias of ~0.3 ppm and slightly improved correlation (R = 0.39) compared to prior model results. Posterior model results for the summer season displayed nearly zero bias and high correlation values of 0.79. The statistical evaluation of posterior model performance in the fall months improved compared to prior simulations with bias ~-0.1 ppm and correlation of 0.57. Finally, for winter months posterior results had bias ~0.1 ppm, a significant improvement from 1.0 ppm from the prior result, and moderate correlation of 0.41. Overall, posterior results from the GP inversion performed in this study proved to be more accurate compared to prior simulations suggesting the emission estimates from these inverse model runs are robust, as expected from the PPCs.

3.4 Posterior emissions by season and sector

We estimate state-wide posterior emissions by season and sector based on Model 1, which was evaluated to perform the best based on the ELPD metric (see Text S1), and the seasonally-averaged posterior emissions are displayed in Fig. 3. Figure 4 shows the seasonal state-wide total posterior CO_2 fluxes from all 3 GP inversion models (̶s̶e̶e̶ ̶T̶e̶x̶t̶ ̶S̶2̶) and the prior estimates for each source sector in California during 2020 (monthly-averaged prior and posterior state-wide CO_2 fluxes displayed in Fig. S8). In general, all 3 GP inversion models are relatively consistent with respect to

369 median posterior emissions estimates for all source sectors and seasons. This consistency suggests that the GP models
370 are robust in inferring posterior emissions, despite slight performance variations by season and sector for each model.
371 The rest of the results discussed in this section are focused on posterior estimates from Model 1. Figure 4 shows that
372 posterior FF emissions align closely with the prior estimates on a seasonal-scale, indicating consistency between the
373 initial assumptions and the inversion-derived results (PDFs for Model 1 shown in Fig. S4). Posterior FF emissions are
374 most consistent with prior estimates during the spring and summer months when COVID-19 lockdown restrictions
375 were most strict, suggesting that corrections applied to the 2020 Vulcan data applying CARB data were accurate
376 reasonable compared to observations. For the fall and winter seasons posterior FF emission estimates were reduced
377 by 10-15 Tg CO_2 compared to a priori assumptions, although the reduction is within the margin of error. Seasonal
378 posterior 2σ uncertainty (95% confidence level) had a range of 20-30 Tg CO_2 which on average is ~30% of the
379 seasonal posterior median FF emission values. Interestingly, from the monthly-averaged state-wide emissions shown
380 in Fig. S8, it can be seen that some months in the spring, summer, and fall of 2020 had posterior FF fluxes further
381 reduced compared to the prior emissions emphasizing the strong reduction in GHG emissions due to COVID-19
382 lockdown restrictions.

383

Figure 3. Seasonally-averaged 2020 posterior CO_2 emissions (µmol m^{-2} sec^{-1}) for the state of California.
Emissions from the terrestrial portion of California are shown for FF (left column), NEE (middle column), and
Fire (right column) for the spring (first row), summer (second row), fall (third row), and winter (fourth row)
months.
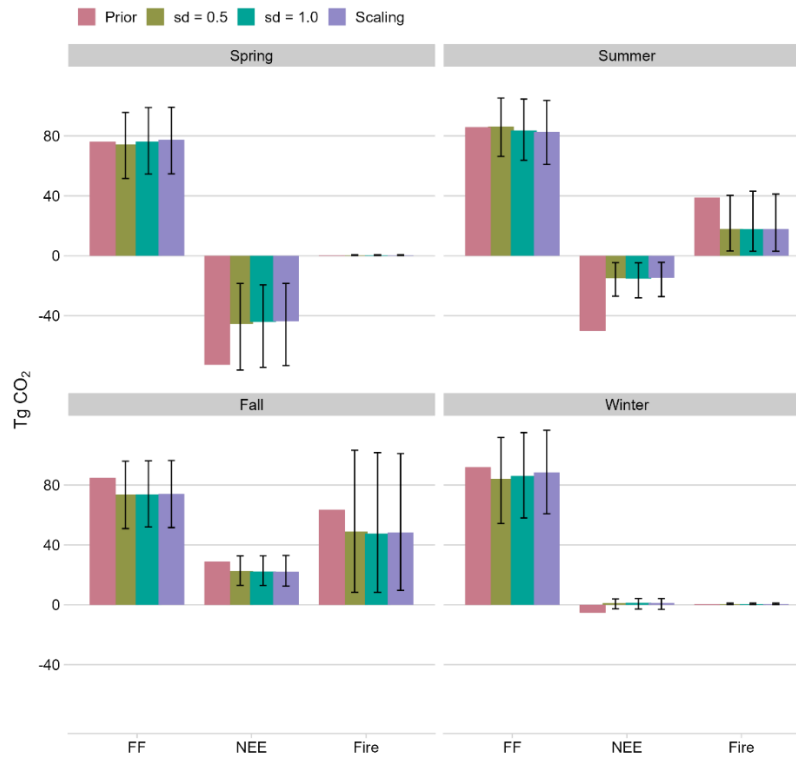
Figure 4. Sectoral emission estimates (Tg CO₂) by season from the scaled Vulcan a priori and those using three distinct models: Model 1 ("sd = 0.5"), where a standard deviation (sd) of 0.5 ppm is applied to the prior probability distribution for the systematic bias; Model 2 ("sd = 1.0"), with a standard deviation of 1.0 ppm for the prior for the systematic bias; and Model 3 ('Scaling'), which optimizes the OCO-2 and OCO-3 a priori and model-predicted BC concentrations using scaling factors analogous to sector emissions adjustments. The error bars in this figure reflect the 2σ uncertainty (i.e., 95% confidence) values for each source sector. All 2σ confidence intervals were calculated using 4000 MCMC samples.

Posterior NEE fluxes from the GP inversion indicate that prior estimates assumed carbon uptake which was too strong during the drought year of 2020, suggesting an overestimation of the ecosystem's carbon sequestration capacity. Besides the fall season, posterior NEE was much less negative compared to the a priori fluxes, and even transitioned from a small sink to a small source during the winter season (see Fig. 3 and 44). Posterior NEE fluxes are 25–35 Tg CO₂ less (lower NEE) compared to prior estimates in the growing seasons of the spring and summer. From Fig. S8 it can be seen that during some of the summer months posterior NEE fluxes were near neutral compared to the large uptake suggested by prior fluxes. This is likely due to the strong drought and hot temperatures experienced in California during 2020 greatly reducing the CO₂ uptake during the growing season. The posterior adjustments during the fall were smaller and tended to be consistent with prior estimates from SMUrF. Posterior NEE emissions were consistent with the prior estimates within a 2σ uncertainty range for the spring and fall seasons; however, were not statistically consistent for winter and summer months. Seasonal posterior NEE ~~values~~ displayed the largest uncertainty values of all source sectors in California and these uncertainties were on average ~95% of the seasonal posterior median emission value.

The inversion results for fire emissions imply that the prior estimates are consistent with the posterior results within the 2σ uncertainty range although the posterior median values for summer were lower than the prior. As expected, prior and posterior CO₂ emissions from fires were small during the winter and spring months. Posterior median seasonal total CO₂ emissions ranged between 20 and 50 Tg CO₂ for the summer and fall seasons, respectively.

413 Constraints from OCO-2 and OCO-3 observations reduced emission estimates compared to the prior during both of
414 these seasons with the largest reduction occurring for summer months (-21%). Seasonal posterior fire emission values
415 displayed moderate to high uncertainty values and these uncertainties were on average ~80% of the seasonal posterior
416 median emission values.

3.5 State-wide posterior total CO$_2$ emissions

418 This section describes the annual state-wide CO$_2$ flux estimates constrained using OCO-2 and OCO-3 observations
419 for each source sector in 2020. Table 2 shows the results of the prior and posterior state-wide flux estimates for each
420 source sector and the overall net terrestrial flux. The PDFs of these annual state-wide CO$_2$ fluxes are displayed in Fig.
421 5 (seasonal sector CO$_2$ flux PDFs shown in Fig. S9). Both the table and figure show that the net state-wide CO$_2$ flux
422 from both prior and posterior estimates are nearly identical ~~around~~ between 340-350 Tg CO$_2$ yr^{-1}. However, larger
423 differences are evident when the state-wide annual emissions are broken down by source sector. Large constraints
424 were imposed by OCO-2 and OCO-3 observations when focusing on NEE fluxes, where the posterior median estimate
425 (-36.8 Tg CO$_2$ yr^{-1}; range of -71.7 – -6.0 Tg CO$_2$ yr^{-1}; 95% confidence level) was 63% lower (reduced carbon sink)
426 compared to prior estimates (-99.2 Tg CO$_2$ yr^{-1}). Prior emissions from wildland fires were also reduced when
427 constrained by satellite observations as state-wide posterior estimates of 68.0 Tg CO$_2$ yr^{-1} (range of 24.9 – 126.2 Tg
428 CO$_2$ yr^{-1}; 95% confidence level) were ~35% lower compared to a priori estimates. Finally, posterior FF emissions
429 were 317.8 Tg CO$_2$ yr^{-1} (range of 271.3 – 364.0 Tg CO$_2$ yr^{-1}; 95% confidence level) which is ~5% lower compared to
430 the prior estimates.

431 **Table 2. Median ~~P~~prior and posterior (~~median~~2σ range; 95% confidence level) California CO$_2$ budget for 2020.**

Source	Prior CO$_2$ Flux (Tg CO$_2$ yr^{-1})	Posterior CO$_2$ Flux (Tg CO$_2$ yr^{-1})
FF	338.4	317.8 (271.3 – 364.0)
NEE	-99.2	-36.8 (71.7 – -6.0)
Fire	103.3	68.0 (24.9 – 126.2)
Total	342.5	349.6 (272.8 – 428.6)

432 For total CO$_2$ fluxes, including all source sectors, California state-wide emissions are constrained with
433 relatively high confidence using OCO-2 and OCO-3 XCO$_2$~~XCO2~~ observations as the 2σ standard deviation on this
434 total flux is ~23% of the annual median posterior estimate. Annual posterior emission estimates were most confident
435 for FF sources as the 2σ standard deviation from these sources was 47 Tg CO$_2$ which is ~15% of the posterior median
436 value. Natural fluxes of CO$_2$ (i.e., NEE and wildland fire) in California displayed higher uncertainties for their
437 posterior estimates indicated by the wider PDFs in Fig. 5. The 2σ standard deviation of annual posterior NEE fluxes
438 was on average ~35 Tg CO$_2$ which is ~95% of the posterior median value indicating this is the most uncertain carbon
439 flux when using satellites to constrain emissions. Posterior annual fire emissions were also associated with larger
440 uncertainty as the 2σ uncertainty range was 43 Tg CO$_2$ (64% of the median posterior flux).

441
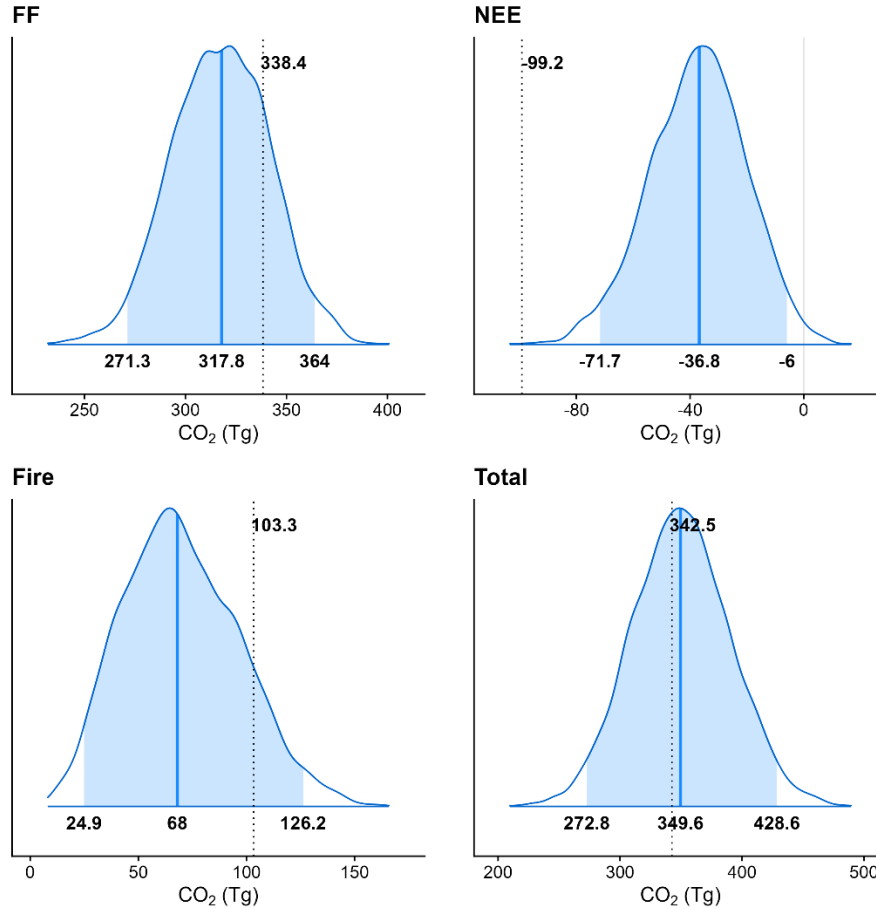
Figure 5. Annual CO₂ emission totals (Tg CO₂) for California by source sector in 2020. The numerical labels at the base of each PDF denote the 2.5ᵗʰ, 50ᵗʰ (indicated by the bold vertical line), and 97.5ᵗʰ percentile estimates of the posterior emissions, respectively. The vertical dotted line indicates the prior emission estimate, with the corresponding value displayed. Note that the annual PDF presented here was derived by aggregating seasonal MCMC samples.

4. Discussion and conclusions

This study presents the first attempt to constrain state-wide CO_2 fluxes from California using spaceborne XCO_2~~XCO2~~ observations using both OCO-2 and OCO-3. We chose to focus on the year 2020 as this time period was characterized by anomalous features likely impacting total CO_2 fluxes in California including: reduced anthropogenic emissions caused by the COVID-19 lockdown (Yañez et al., 2022), elevated wildfire activity (Jerret et al., 2022; Safford et al., 2022), and drought occurrence (Steel et al., 2022). Assimilating OCO-2 and OCO-3 LN+LG XCO_2~~XCO2~~ observations into a GP inversion framework was demonstrated in this study to be effective for constraining state-wide CO_2 fluxes with a high degree of accuracy. The median posterior top-down annual total CO_2 flux of 349.6 Tg CO_2 yr⁻¹ (range of 272.8 – 428.6 Tg CO_2 yr⁻¹; 95% confidence level) was consistent with the a priori estimate and constrained with low 2σ uncertainty levels of ~23%. The posterior uncertainty estimates of this study are similar to other recent research that have used OCO-2 and OCO-3 XCO_2~~XCO2~~ data to constrain city-wide CO_2 emissions in California (e.g., Roten et al., 2023), other city flux estimates (e.g., Wu et al., 2020), and country-wide CO_2 budgets (e.g., Byrne et al., 2023). Our study adds to the growing evidence of how satellite XCO_2~~XCO2~~ data can be used to confidently estimate city- to country-scale CO_2 fluxes.

461   CARB inventories for the years 2019 and 2020 suggest that anthropogenic FF CO_2 emissions were reduced
462   by ~10% in 2020 compared to the year prior in California. The state-wide annual FF CO_2 source was estimated in this
463   study using the GP inversion assimilating OCO-2 and OCO-3 XCO2~~XCO2~~ data for 2020 to be 317.8 Tg CO_2 yr^{-1}
464   which is ~5% lower than the prior flux assumed. This top-down estimate is ~15% higher compared to the CARB 2020
465   inventory which ~~suggests~~ calculated state-wide anthropogenic CO_2 emissions for 2020 ~~were~~ to be 277.7 Tg CO_2 yr^{-1}.
466   The state-wide FF CO_2 emissions estimated using OCO-2 and OCO-3 data in this study had posterior uncertainties of
467   ~15% on an annual-scale and therefore is statistically consistent with the CARB 2020 inventory. The difference
468   between the bottom-up and top-down median FF CO_2 emission estimate may be due to errors and uncertainties in the
469   GP inversion and errors in the bottom-up CARB inventory such as missing sources. It appears the results in our study
470   for FF emission estimates are robust as they compare well to year 2020 emission totals in California from CARB and
471   posterior top-down estimates are associated with low posterior uncertainty. Our PPC results, which compare the
472   simulated data from posterior parameters with observations, provide additional confidence in our GP inversion
473   models.

474   The main natural sources/sinks of CO_2 in California (i.e., NEE and wildland fire) were also estimated in this
475   study using OCO-2 and OCO-3 XCO2~~XCO2~~ data. The year 2020 was a year of drought in California and also resulted
476   in extremely large wildfire activity. The GP inversion resulted in posterior NEE fluxes which were greatly reduced
477   compared to the initial best guess a priori data. On an annual-scale, the posterior estimate for NEE was -36.8 Tg CO_2
478   yr^{-1} which was 63% lower (reduced carbon sink) compared to prior estimates driven by satellite SIF retrievals. It is
479   important to note that 2020 was towards the end of a multi-year drought that plagued California and it would be
480   expected that the terrestrial biosphere would be less effective in its uptake of carbon (Fu et al., 2022). It should also
481   be noted that the median annual posterior NEE estimates derived in this study with satellite retrievals were associated
482   with uncertainty levels of ~95%. The larger uncertainty value associated with our posterior NEE estimates, compared
483   to FF sources, is expected as satellite retrievals are less sensitive to small diffuse signals of CO_2 enhancements
484   associated with the terrestrial biosphere compared to larger FF point-sources. Wildfire activity was elevated in
485   California during the time of this study, and we estimated that these sources contributed 68.0 Tg CO_2 yr^{-1} to the total
486   state-wide annual carbon budget. The posterior estimate derived in our GP inversion was ~35% lower compared to
487   prior estimate; however, this estimate still represents highly elevated CO_2 emissions from this natural source. CARB
488   estimated that ~100 Tg CO_2 yr^{-1} was emitted from wildfires in 2020 (https://ww2.arb.ca.gov/wildfire-emissions)
489   which is in line with the prior estimate from GFED4 used in our study. CARB uses an emissions model which is
490   similar to GFED4 so this is to be expected. The lower posterior wildfire estimate using our GP inversion system was
491   associated with uncertainty levels (~64% of the median posterior flux) lower compared to NEE and were statistically
492   consistent with the CARB 2020 state-wide estimate. Prior emission estimates from wildfires are generally uncertain
493   and satellite observations of the CO_2 resulting from these episodic events are challenging; thus, it is not surprising that
494   posterior fire emissions are one of the more uncertain components of the 2020 California CO_2 budget.

495   ~~In evaluating the GP inversion method used in this study compared to linear inverse models (e.g., $y=K\lambda+c$,~~
496   ~~commonly used in atmospheric inversions; (Rodgers, 2000)), advantages and disadvantages become apparent. The~~
497   ~~GP inversion offers substantial flexibility in modeling intricate, non-linear dependencies without needing a pre-~~
498   ~~specified model framework (Ebden, 2015). Thus, instead of confining the unknown function f to fixed models, the~~
499   ~~GP model allows it to be defined more indirectly yet robustly. Note that we use $K\lambda$ (adjusted model predictions) as~~
500   ~~the mean function in Eq. (5) and do not equate it directly with the unknown function f. Thus, the GP approach treats~~
501   ~~the function f as a random function, which can be sampled from a joint Gaussian distribution, allowing for greater~~
502   ~~flexibility in fitting data compared to traditional linear inverse models. In contrast to the linear inverse model (e.g.,~~
503   ~~represented as $y=K\lambda+c$), which does not account for interactions between variables, the GP model can implicitly~~
504   ~~capture interactions among input features through its choice of kernel. Also, the GP inversion intrinsically provides~~
505   ~~quantification of uncertainty, which proves advantageous in scenarios with limited data as in atmospheric inversions.~~
506   ~~However, the computational demands of the GP method increase significantly with larger datasets, potentially~~
507   ~~restricting its application in certain contexts (Williams and Rasmussen, 2006; Murphy, 2022), although recent~~
508   ~~development for high-performance computing (e.g., GPU-enabled tools) can alleviate this issue. Conversely, the linear~~

509 ~~inverse model, while less computationally demanding, assumes linearity and typically requires explicit assumptions~~
510 ~~about the underlying distribution, which may not always be valid and can lead to underestimation of model uncertainty~~
511 ~~(Wang, 2023).~~

512 Given that individual state- and country-wide CO_2 flux data sets generally have over a year of latency,
513 satellite data becomes vital as this spaceborne data is well equipped to provide more real-time estimates of these
514 emissions. This is an important aspect of satellite data especially during times of anomalous CO_2 fluxes due to
515 economic activity, wildfire, or flood/drought. Both this study and the work by Roten et al. (2023) clearly demonstrated
516 the ability of OCO-2, and in particular OCO-3, to help constrain FF emission estimates in California during the
517 COVID-19 lockdown. OCO-3 is particularly effective for estimating city-wide, or other point- to area-source, fluxes
518 using the data extracted from SAMs. These area wide observations (~80 km $\times$ 80 km) greatly improve the
519 observational coverage compared to OCO-2 (narrow swath of only ~10 km). These SAMs allow for observations
520 which reduce errors in assumptions about mixing between the sources and observations and illustrate intra-city
521 variability of XCO_2 which was shown to allow for sector-based emission constraints in California (Roten et al., 2023).
522 The recent launch of satellites, and future plans for spaceborne instruments, which retrieve greenhouse gas
523 concentrations (e.g., GHGSat, CO2M, Carbon Mapper, etc.) at high spatial resolution and precision, some of which
524 will apply SAM observational approaches, should greatly improve the ability to accurately estimate CO_2 emissions
525 from city- to global-scales. As demonstrated, our GP inverse model has the potential to utilize these new satellite data
526 sets to estimate surface emissions in near-real-time fashion, effectively incorporating the unique spatiotemporal
527 coverage of space-based information.

528 In evaluating the GP inversion method used in this study compared to linear inverse classical Bayesian
529 inversion (CBI) models (~~[~~e.g., $\mathbf{y}=\mathbf{K}\lambda+\epsilon$, commonly used in atmospheric inversions; (Rodgers, 2000)~~)~~], advantages and
530 disadvantages become apparent. The GP-based inversion method employed in this work offers several advantages
531 over classical methods, as highlighted by Jeong et al. (2025). Jeong et al. (2025) presents the advantages of the GP
532 method through inversion results from different approaches, and we briefly describe them here, focusing on the key
533 points.

534 First, Jeong et al. (2025) demonstrated through simulations using multiple inverse modeling methods for
535 constraining CO_2 fluxes in California when assimilating OCO-2+OCO-3 XCO_2 observations that the GP inversion
536 yields superior results compared to the CBI method. Specifically, the CBI method failed to capture the FF scaling
537 factor accurately at the 68% confidence level. They repeated the inversion multiple times, and this result was
538 consistent. Their work also showed that without a proper prior distribution, a simple linear regression produced a
539 physically implausible scaling factor for fire emissions. In our full Bayesian approach, we specify prior distributions
540 for all parameters, including the scaling factors and kernel hyperparameters. Overall, ~~T~~the GP inversion offers
541 substantial flexibility in modeling intricate, non-linear dependencies without needing a pre-specified model
542 framework (Ebden, 2015).

543 Second, the CBI method typically relies on analytical solutions and lacks robust techniques for estimating
544 crucial parameters, such as hyperparameters (e.g., variance of the diagonal elements) for the covariance matrix (i.e.,
545 the kernel). Consequently, many previous inversion studies have used prescribed values for hyperparameters. For
546 instance, these studies often utilized known values from other work (e.g., Roten et al., 2023) or estimations derived
547 from sensitivity analyses to construct the model-data mismatch covariance (Gerbig et al., 2003; Jeong et al., 2013;
548 Johnson et al., 2016). Such approaches do not guarantee that the estimates are consistent with the observed data. In
549 contrast, Jeong et al. (2025) showed that the GP method can infer the noise variance, with its median value closely
550 aligning with the true value. This represents a significant advancement over previous approaches, as it enables the
551 direct estimation of true noise variance from the input data. Also, the GP inversion intrinsically provides quantification
552 of uncertainty, which proves advantageous in scenarios with limited data as in atmospheric inversions.

553 Third, the GP method includes the spatiotemporal kernel as its essential component, as shown in this work.
554 While some previous work (e.g., Turner et al., 2020) used a covariance with both spatial and temporal components,

many previous inversion studies have not used a fully spatiotemporal covariance. This is because it is not straightforward to estimate the hyperparameters for the spatiotemporal covariance in the CBI method based on analytical solutions (Jeong et al., 2025). For example, the work by Turner et al. (2020) did not estimate the covariance parameters in a way consistent with the data. Incorporating the spatiotemporal covariance as a core component of the inversion is a significant advantage of the GP method over the CBI method.

~~However~~While the GP-based inversion has many advantages over CBI methods, the computational demands of the GP method increase significantly with larger datasets, potentially restricting its application in certain contexts (Williams and Rasmussen, 2006; Murphy, 2022), although recent development for high-performance computing (e.g., GPU-enabled tools) can alleviate this issue. Conversely, the linear inverse model, while less computationally demanding, assumes linearity and typically requires explicit assumptions about the underlying distribution, which may not always be valid and can lead to underestimation of model uncertainty (Wang, 2023). Overall, this study demonstrates the clear advantages of using GP-based inversion techniques and this modeling framework should be considered for application in future studies for constraining GHG fluxes when assimilating satellite retrievals.

~~Given that individual state- and country-wide CO_2 flux data sets generally have over a year of latency, satellite data becomes vital as this spaceborne data is well-equipped to provide more real-time estimates of these emissions. This is an important aspect of satellite data especially during times of anomalous CO_2 fluxes due to economic activity, wildfire, or flood/drought. Both this study and the work by Roten et al. (2023) clearly demonstrated the ability of OCO-2, and in particular OCO-3, to help constrain FF emission estimates in California during the COVID-19 lockdown. OCO-3 is particularly effective for estimating city-wide, or other point- to area-source, fluxes using the data extracted from SAMs. These area-wide observations (~80 km × 80 km) greatly improve the observational coverage compared to OCO-2 (narrow swath of only ~10 km). These SAMs allow for observations which reduce errors in assumptions about mixing between the sources and observations and illustrate intra-city variability of XCO2 which was shown to allow for sector-based emission constraints in California (Roten et al., 2023). The recent launch of satellites, and future plans for spaceborne instruments, which retrieve greenhouse gas concentrations (e.g., GHGSat, CO2M, Carbon Mapper, etc.) at high spatial resolution and precision, some of which will apply SAM observational approaches, should greatly improve the ability to accurately estimate CO_2 emissions from city- to global-scales. As demonstrated, our GP inverse model has the potential to utilize these new satellite data sets to estimate surface emissions in near-real-time fashion, effectively incorporating the unique spatiotemporal coverage of space-based information.~~

Code and Data Availability. The NASA OCO-3 Level 2 bias-corrected version 10.4r and OCO-2 Level 2 bias-corrected version 11r data are available from https://disc.gsfc.nasa.gov/ (last access: 15 June 2023). The Vulcan version 3.0 high-resolution hourly dataset is available at https://daac.ornl.gov/cgi-bin/dsviewer.pl?ds_id=1810 (last access: 27 September 2022). The CARB California GHG Emission inventory is available at https://ww2.arb.ca.gov/ghg-inventory-data (last access: 2 November 2022). Carbon dioxide fluxes from CarbonTracker are available from https://gml.noaa.gov/aftp/products/carbontracker/co2/CT-NRT.v2022-1/fluxes/daily/ (last access: 14 March 2024). Biogenic fluxes from the SMUrF model are available from http://dienwu.me/gmd2021/ (last access: 29 March 2023). Fire emissions data is available from https://doi.org/10.5281/zenodo.7229674 (last access: 1 February 2023). The GEOS-Chem model is openly available to the public and can be downloaded at https://zenodo.org/records/12584192 (last access: 11 September 2023).

Supplement. The supplement related to this article is available.

Author Contributions. SJ ~~and MF were~~ was responsible for obtaining the funding which supported this project. MSJ, SDH, SJ, and M~~L~~F conceived the overall project ideas. MSJ, YC, and SJ performed the GEOS-Chem and GP model

597 simulations which produced the majority of the results presented in this study. DW, AT, and SDH provided critical
598 bottom-up emission data sets used throughout the study. MSJ and SJ were responsible for writing the manuscript with
599 the aid of all coauthors.

600 *Competing interests.* The authors declare that they have no conflict of interest.

601 *Acknowledgements.* Computational resources were provided by the NASA High-End Computing Program through the
602 NASA Advanced Supercomputing Division at NASA Ames Research Center and Computing Allowance Program at
603 Lawrence Berkeley National Laboratory from the Lawrencium Cluster. The views, opinions and findings of this paper
604 are those of the authors and should not be construed as an official NASA or United States Government position,
605 policy, or decision.

606 *Financial support.* MSJ, SDH, SJ, DW, AT, and MF acknowledge funding support from the NASA Earth Science
607 Division's Carbon Cycle Science Program (grant number: *80HQTR21T0101*) YC contributions to this work were
608 through in-kind efforts.

References

Abril-Pla, O., Andreani, V., Carroll, C., Dong, L., Fonnesbeck, C. J., Kochurov, M., et al.: PyMC: a modern, and comprehensive probabilistic programming framework in Python, PeerJ Computer Science, 9, e1516. doi:10.7717/peerj-cs.1516, 2023.

Andres, R. J., Boden, T. A., Bréon, F.-M., Ciais, P., Davis, S., Erickson, D., Gregg, J. S., Jacobson, A., Marland, G., Miller, J., Oda, T., Olivier, J. G. J., Raupach, M. R., Rayner, P., and Treanton, K.: A synthesis of carbon dioxide emissions from fossil-fuel combustion, Biogeosciences, 9, 1845–1871, https://doi.org/10.5194/bg-9-1845-2012, 2012.

Baker, D. F., Bell, E., Davis, K. J., Campbell, J. F., Lin, B., and Dobler, J.: A new exponentially decaying error correlation model for assimilating OCO-2 column-average CO2 data using a length scale computed from airborne lidar measurements, Geosci. Model Dev., 15, 649–668, https://doi.org/10.5194/gmd-15-649-2022, 2022.

Bevilacqua, M., Caamaño-Carrillo, C., and Porcu, E.: Unifying compactly supported and Matérn covariance functions in spatial statistics, Journal of Multivariate Analysis, 189, 104949, doi:10.1016/j.jmva.2022.104949, 2022.

Bey, I., Jacob, D. J., Yantosca, R. M., Logan, J. A., Field, B. D., Fiore, A. M., Li, Q. B., Liu, H. G. Y., Mickley, L. J., and Schultz, M. G.: Global modeling of tropospheric chemistry with assimilated meteorology: Model description and evaluation, J. Geophys. Res.-Atmos., 106, 23073–23095, https://doi.org/10.1029/2001JD000807, 2001.

Biship, C. M.: Pattern Recognition and Machine Learning (Information Science and Statistics); Springer: Berlin/Heidelberg, Germany, 2007.

Bousserez, N., Henze, D.K., Perkins, A., Bowman, K.W., Lee, M., Liu, J., Deng, F., and Jones, D. B. A.: Improved analysis error covariance matrix for high-dimensional variational inversions: application to source estimation using a 3D atmospheric transport model, Q. J. Roy. Meteor. Soc., 141, 1906–1921, https://doi.org/10.1002/qj.2495, 2015.

Byrne, B., Baker, D. F., Basu, S., Bertolacci, M., Bowman, K. W., Carroll, D., Chatterjee, A., Chevallier, F., Ciais, P., Cressie, N., Crisp, D., Crowell, S., Deng, F., Deng, Z., Deutscher, N. M., Dubey, M. K., Feng, S., García, O. E., Griffith, D. W. T., Herkommer, B., Hu, L., Jacobson, A. R., Janardanan, R., Jeong, S., Johnson, M. S., Jones, D. B. A., Kivi, R., Liu, J., Liu, Z., Maksyutov, S., Miller, J. B., Miller, S. M., Morino, I, Notholt, J., Oda, T., O'Dell, C. W., Oh, Y.-S., Ohyama, H., Patra, P. K., Peiro, H., Petri, C., Philip, S., Pollard, D. F., Poulter, B., Remaud, M., Schuh, A., Sha, M. K., Shiomi, K., Strong, K., Sweeney, C., Té, Y., Tian, H., Velazco, V. A., Vrekoussis, M., Warneke, T., Worden, J. R., Wunch, D., Yao, Y., Yun, J., Zammit-Mangion, A., and Zeng, N.: National CO2 budgets (2015–2020) inferred from atmospheric CO2 observations in support of the global stocktake, Earth Syst. Sci. Data, 15, 963–1004, https://doi.org/10.5194/essd-15-963-2023, 2023.

California Air Resources Board: GHG Emissions Inventory (GHG EI) 2000-2020, https://ww2.arb.ca.gov/ghg-inventory-data (last access: March 15, 2024), 2022.

California Air Resources Board: California Greenhouse Gas Emissions from 2000 to 2021: Trends of Emissions and Other Indicators, https://ww2.arb.ca.gov/ghg-inventory-data (last access: December 21, 2023), 2023.

Crisp, D., Pollock, H. R., Rosenberg, R., Chapsky, L., Lee, R. A. M., Oyafuso, F. A., Frankenberg, C., O'Dell, C. W., Bruegge, C. J., Doran, G. B., Eldering, A., Fisher, B. M., Fu, D., Gunson, M. R., Mandrake, L., Osterman, G. B., Schwandner, F. M., Sun, K., Taylor, T. E., Wennberg, P. O., and Wunch, D.: The on-orbit performance of the Orbiting Carbon Observatory-2 (OCO-2) instrument and its radiometrically calibrated products, Atmos. Meas. Tech., 10, 59–81, https://doi.org/10.5194/amt-10-59-2017, 2017.

Cui, X., Newman, S., Xu, X., Andrews, A. E., Miller, J., and Lehman, S.: Atmospheric observation-based estimation of fossil fuel CO2 emissions from regions of central and southern California, Sci. Total Environ., 664, 381–391, https://doi.org/10.1016/j.scitotenv.2019.01.081, 2019.

Cui, Y. Y., L. Zhang, A. R. Jacobson, M. S. Johnson, S. Philip, D. Baker, et al.: Evaluating global atmospheric inversions of terrestrial net ecosystem exchange CO$_2$ over North America on seasonal and sub-continental scales. Geophysical Research Letters, 49, e2022GL100147. https://doi.org/10.1029/2022GL100147, 2022.

Dunn, R. J. H., F. Aldred, N. Gobron, J. B Miller, and K. M. Willett, Eds.: Global Climate [in "State of the Climate in 2021"]. Bull. Amer. Meteor. Soc., 103 (8), S11–S142, https://doi.org/10.1175/BAMS-D-22-0092.1, 2022.

Ebden, M.: Gaussian Processes: A Quick Introduction, arXiv:1505.02965v2 [math.ST], 2015.

Eldering, A., Taylor, T. E., O'Dell, C. W., and Pavlick, R.: The OCO-3 mission: measurement objectives and expected performance based on 1 year of simulated data, Atmos. Meas. Tech., 12, 2341–2370, https://doi.org/10.5194/amt-12-2341-2019, 2019.

Fischer, M. L., Parazoo, N., Brophy, K., Cui, X., Jeong, S., Liu, J., Keeling, R., Taylor, T. E., Gurney, K., Oda, T., and Graven, H.: Simulating estimation of California fossil fuel and biosphere carbon dioxide exchanges combining in situ tower and satellite column observations, J. Geophys. Res.-Atmos., 122, 3653–3671, https://doi.org/10.1002/2016JD025617, 2017.

Friedlingstein, P., O'Sullivan, M., Jones, M. W., Andrew, R. M., Bakker, D. C. E., Hauck, J., Landschützer, P., Le Quéré, C., Luijkx, I. T., Peters, G. P., Peters, W., Pongratz, J., Schwingshackl, C., Sitch, S., Canadell, J. G., Ciais, P., Jackson, R. B., Alin, S. R., Anthoni, P., Barbero, L., Bates, N. R., Becker, M., Bellouin, N., Decharme, B., Bopp, L., Brasika, I. B. M., Cadule, P., Chamberlain, M. A., Chandra, N., Chau, T.-T.-T., Chevallier, F., Chini, L. P., Cronin, M., Dou, X., Enyo, K., Evans, W., Falk, S., Feely, R. A., Feng, L., Ford, D. J., Gasser, T., Ghattas, J., Gkritzalis, T., Grassi, G., Gregor, L., Gruber, N., Gürses, Ö., Harris, I., Hefner, M., Heinke, J., Houghton, R. A., Hurtt, G. C., Iida, Y., Ilyina, T., Jacobson, A. R., Jain, A., Jarníková, T., Jersild, A., Jiang, F., Jin, Z., Joos, F., Kato, E., Keeling, R. F., Kennedy, D., Klein Goldewijk, K., Knauer, J., Korsbakken, J. I., Körtzinger, A., Lan, X., Lefèvre, N., Li, H., Liu, J., Liu, Z., Ma, L., Marland, G., Mayot, N., McGuire, P. C., McKinley, G. A., Meyer, G., Morgan, E. J., Munro, D. R., Nakaoka, S.-I., Niwa, Y., O'Brien, K. M., Olsen, A., Omar, A. M., Ono, T., Paulsen, M., Pierrot, D., Pocock, K., Poulter, B., Powis, C. M., Rehder, G., Resplandy, L., Robertson, E., Rödenbeck, C., Rosan, T. M., Schwinger, J., Séférian, R., Smallman, T. L., Smith, S. M., Sospedra-Alfonso, R., Sun, Q., Sutton, A. J., Sweeney, C., Takao, S., Tans, P. P., Tian, H., Tilbrook, B., Tsujino, H., Tubiello, F., van der Werf, G. R., van Ooijen, E., Wanninkhof, R., Watanabe, M., Wimart-Rousseau, C., Yang, D., Yang, X., Yuan, W., Yue, X., Zaehle, S., Zeng, J., and Zheng, B.: Global Carbon Budget 2023, Earth Syst. Sci. Data, 15, 5301–5369, https://doi.org/10.5194/essd-15-5301-2023, 2023.

Fu, Z., Ciais, P., Prentice, I. C., Gentine, P., Makowski, D., Bastos, A., Luo, X., Green, J. K., Stoy, P. C., Yang, H., and Hajima, T.: Atmospheric dryness reduces photosynthesis along a large range of soil water deficits, Nat. Commun., 13, 989, https://doi.org/10.1038/s41467-022-28652-7, 2022.

Ganesan, A. L., Rigby, M., Zammit-Mangion, A., Manning, A. J., Prinn, R. G., Fraser, P. J., Harth, C. M., Kim, K.-R., Krummel, P. B., Li, S., Mühle, J., O'Doherty, S. J., Park, S., Salameh, P. K., Steele, L. P., and Weiss, R. F.: Characterization of uncertainties in atmospheric trace gas inversions using hierarchical Bayesian methods, Atmos. Chem. Phys., 14, 3855–3864, https://doi.org/10.5194/acp-14-3855-2014, 2014.

Ganesan, A. L., Manning, A. J., Grant, A., Young, D., Oram, D. E., Sturges, W. T., Moncrieff, J. B., and O'Doherty, S.: Quantifying methane and nitrous oxide emissions from the UK and Ireland using a national-scale monitoring network, Atmos. Chem. Phys., 15, 6393–6406, https://doi.org/10.5194/acp-15-6393-2015, 2015.

Gelman, A., Meng, X. L., and Stern, H.: Posterior predictive assessment of model fitness via realized discrepancies, Statistica sinica, 733-760, 1996.

Gerbig, C., Lin, J. C., Wofsy, S. C., Daube, B. C., Andrews, A. E., Stephens, B. B., Bakwin, P. S., and Grainger, C. A.: Toward constraining regional-scale fluxes of CO_2 with atmospheric observations over a continent: 2. Analysis of COBRA data using a receptor-oriented framework, J. Geophys. Res., 108, 4757, https://doi.org/10.1029/2003JD003770, 2003.

Graven, H., Fischer, M. L., Lueker, T., Jeong, S., Guilderson, T. P., Keeling, R. F., Bambha, R., Brophy, K., Callahan, W., Cui, X., Frankenberg, C., Gurney, K. R., LaFranchi, B. W., Lehman, S. J., Michelsen, H., Miller, J. B., Newman, S., Paplawsky, W., Parazoo, N. C., Sloop, C., and Walker, S. J.: Assessing fossil fuel CO2 emissions in California using atmospheric observations and models, Environ. Res. Lett., 13, 065007, https://doi.org/10.1088/1748-9326/aabd43, 2018.

Gulev, S. K., Thorne, P. W., Ahn, J., Dentener, F. J., Domingues, C. M., Gerland, S., Gong, D. S., Kaufman, S., Nnamchi, H. C., Quaas, J., Rivera, J. A., Sathyendranath, S., Smith, S. L., Trewin, B., von Shuckmann, K., and Vose, R. S.: Changing State of the Climate System. In: Climate Change 2021: The Physical Science Basis. Contribution of Working Group I to the Sixth Assessment Report of the Intergovernmental Panel on Climate Change [Masson-Delmotte, V., Zhai, P., Pirani, A., Connors, S. L., Péan, C., Berger, S., Caud, N., Chen, Y., Goldfarb, L., Gomis, M. I., Huang, M., Leitzell, K., Lonnoy, E., Matthews, J. B. R., Maycock, T.K., Waterfield,

T., Yelekçi, O., Yu, R., and Zhou, B. (Eds.)]. Cambridge University Press, Cambridge, United Kingdom and New York, NY, USA, 287–422, https://doi.org/10.1017/9781009157896.004, 2021.

Gurney, K. R., Liang, J., Patarasuk, R., 665 Song, Y., Huang, J., and Roest, G.: The Vulcan Version 3.0 High-Resolution Fossil Fuel CO_2 Emissions for the United States, Journal of Geophysical Research: Atmospheres, 125, https://doi.org/10.1029/2020jd032974, 2020.

Hedelius, J. K., Liu, J., Oda, T., Maksyutov, S., Roehl, C. M., Iraci, L. T., Podolske, J. R., Hillyard, P. W., Liang, J., Gurney, K. R., Wunch, D., and Wennberg, P. O.: Southern California megacity CO2, CH4, and CO flux estimates using ground- and space-based remote sensing and a Lagrangian model, Atmos. Chem. Phys., 18, 16271–16291, https://doi.org/10.5194/acp-18-16271-2018, 2018.

Hoffman, M. D., and Gelman, A.: The No-U-Turn sampler: adaptively setting path lengths in Hamiltonian Monte Carlo, J. Mach. Learn. Res., 15(1), 1593-1623, 2014.

Imasu, R., Matsunaga, T., Nakajima, M., Yoshida, Y., Shiomi, K., Morino, I., Saitoh, N., Niwa, Y., Someya, Y., Oishi, Y., Hashimoto, M., Noda, H., Hikosaka, K., Uchino, O., Maksyutov, S., Takagi, H., Ishida, H., Nakajima, T. Y., Nakajima, T., and Shi, C.:Greenhouse gases Observing SATellite 2 (GOSAT-2): mission overview, Progress in Earth and Planetary Science, 10, 33, https://doi.org/10.1186/s40645-023-00562-2, 2023.

Jacobson, A. R., Schuldt, K. N., Tans, P., Arlyn Andrews, Miller, J. B., Oda, T., Mund, J., Weir, B., Ott, L., Aalto, T., Abshire, J. B., Aikin, K., Aoki, S., Apadula, F., Arnold, S., Baier, B., Bartyzel, J., Beyersdorf, A., Biermann, T., Biraud, S. C., Boenisch, H., Brailsford, G., Brand, W. A., Chen, G., Huilin Chen, Lukasz Chmura, Clark, S., Colomb, A., Commane, R., Conil, S., Couret, C., Cox, A., Cristofanelli, P., Cuevas, E., Curcoll, R., Daube, B., Davis, K. J., De Wekker, S., Coletta, J. D., Delmotte, M., DiGangi, E., DiGangi, J. P., Di Sarra, A. G., Dlugokencky, E., Elkins, J. W., Emmenegger, L., Shuangxi Fang, Fischer, M. L., Forster, G., Frumau, A., Galkowski, M., Gatti, L. V., Gehrlein, T., Gerbig, C., Francois Gheusi, Gloor, E., Gomez-Trueba, V., Goto, D., Griffis, T., Hammer, S., Hanson, C., Haszpra, L., Hatakka, J., Heimann, M., Heliasz, M., Hensen, A., Hermansen, O., Hintsa, E., Holst, J., Ivakhov, V., Jaffe, D. A., Jordan, A., Joubert, W., Karion, A., Kawa, S. R., Kazan, V., Keeling, R. F., Keronen, P., Kneuer, T., Kolari, P., Kateřina Komínková, Kort, E., Kozlova, E., Krummel, P., Kubistin, D., Labuschagne, C., Lam, D. H. Y., Lan, X., Langenfelds, R. L., Laurent, O., Laurila, T., Lauvaux, T., Lavric, J., Law, B. E., Lee, J., Lee, O. S. M., Lehner, I., Lehtinen, K., Leppert, R., Leskinen, A., Leuenberger, M., Levin, I., Levula, J., Lin, J., Lindauer, M., Loh, Z., Lopez, M., Luijkx, I. T., Lunder, C. R., Machida, T., Mammarella, I., Manca, G., Manning, A., Manning, A., Marek, M. V., Martin, M. Y., Matsueda, H., McKain, K., Meijer, H., Meinhardt, F., Merchant, L., Mihalopoulos, N., Miles, N. L., Miller, C. E., Mitchell, L., Mölder, M., Montzka, S., Moore, F., Moossen, H., Morgan, E., Morgui, J.-A., Morimoto, S., Müller-Williams, J., Munger, J. W., Munro, D., Myhre, C. L., Nakaoka, S.-I., Necki, J., Newman, S., Nichol, S., Niwa, Y., Obersteiner, F., O'Doherty, S., Paplawsky, B., Peischl, J., Peltola, O., Piacentino, S., Pichon, J.-M., Pickers, P., Piper, S., Pitt, J., Plass-Dülmer, C., Platt, S. M., Prinzivalli, S., Ramonet, M., Ramos, R., Reyes-Sanchez, E., Richardson, S. J., Riris, H., Rivas, P. P., Ryerson, T., Saito, K., Sargent, M., Sasakawa, M., Scheeren, B., Schuck, T., Schumacher, M., Seifert, T., Sha, M. K., Shepson, P., Shook, M., Sloop, C. D., Smith, P., Stanley, K., Steinbacher, M., Stephens, B., Sweeney, C., Thoning, K.,Timas, H., Torn, M., Tørseth, K., Trisolino, P., Turnbull, J., van den Bulk, P., van Dinther, D., Vermeulen, A., Viner, B., Vitkova, G., Walker, S., Watson, A., Wofsy, S. C., Worsey, J., Worthy, D., Young, D., Zaehle, S., Zahn, A., and Zimnoch, M.: CarbonTracker CT2022, https://doi.org/10.25925/Z1GJ-3254, 2023.

Jeong, S., Hsu, Y. K., Andrews, A. E., Bianco, L., Vaca, P., Wilczak, J. M., and Fischer, M. L.: A multitower measurement network estimate of California's methane emissions, J. Geophys. Res.-Atmos., 118, 11339–11351, 2013.

Jeong, S., Newman, S., Zhang, J., Andrews, A. E., Bianco, L., Bagley, J., Cui, X., Graven, H., Kim, J., Salameh, P., LaFranchi, B. W., Priest, C., Campos-Pineda, M., Novakovskaia, E., Sloop, C. D., Michelsen, H. A., Bambha, R. P., Weiss, R. F., Keeling, R., and Fischer, M. L.: Estimating methane emissions in California's urban and rural regions using multitower observations, J. Geophys. Res.-Atmos., 121, 13031–13049, https://doi.org/10.1002/2016JD025404, 2016.

Jeong, S., Cui, X., Blake, D. R., Miller, B., Montzka, S. A., Andrews, A., Guha, A., Martien, P., Bambha, R. P., LaFranchi, B., Michelsen, H. A., Clements, C. B., Glaize, P., and Fischer, M. L.: Estimating methane emissions from biological and fossil-fuel sources in the San Francisco Bay Area, Geophys. Res. Lett., 44, 1, 486–495, https://doi.org/10.1002/2016GL071794, 2017.

Jeong, S., Newman, S., Zhang, J., Andrews, A. E., Bianco, L., Dlugokencky, E., Bagley, J., Cui, X., Priest, C., Campos-Pineda, M., and Fischer, M. L.: Inverse Estimation of an Annual Cycle of California's Nitrous Oxide Emissions. Journal of Geophysical Research: Atmospheres, 123(9), 4758-4771, https://doi.org/10.1029/2017JD028166, 2018.

Jeong, S., Hamilton, S. D., Johnson, M. S., Wu, D., Turner, A. J., and Fischer, M. L.: Applying Gaussian Process Machine Learning and Modern Probabilistic Programming to Satellite Data to Infer CO_2 Emissions. Environmental Science & Technology, 59, 9, 4376–4387, https://doi.org/10.1021/acs.est.4c09395, 2025.

Jerret, M., Jina, A. S., and Marlier, M. E.: Up in smoke: California's greenhouse gas reductions could be wiped out by 2020 wildfires, Environmental Pollution, 310, 119888, https://doi.org/10.1016/j.envpol.2022.119888, 2022.

Johnson, M. S., Xi, X., Jeong, S., Yates, E. L., Iraci, L. T., Tanaka, T., Loewenstein, M., Tadic, J. M., and Fischer, M. L.: Investigating seasonal methane emissions in Northern California using airborne measurements and inverse modeling, J. Geophys. Res.-Atmos., 121, 13753–13767, https://doi.org/10.1002/2016JD025157, 2016.

Keeley, J. and Syphard, A.: Large California wildfires: 2020 fires in historical context, Fire Ecol., 17, 22, https://doi.org/10.1186/s42408-021-00110-7, 2021.

Kiel, M., Eldering, A., Roten, D. D., Lin, J. C., Feng, S., Lei, R., Lauvaux, T., Oda, T., Roehl, C. M., Blavier, J.-F., and Iraci, L. T.: Urban-focused satellite CO2 observations from the Orbiting Carbon Observatory-3: A first look at the Los Angeles megacity, Remote Sens. Environ., 258, 112314, https://doi.org/10.1016/j.rse.2021.112314, 2021.

Lan, X., Tans, P., and Thoning, K. W.: Trends in globally-averaged CO_2 determined from NOAA Global Monitoring Laboratory measurements, Version 2023-09. National Oceanic and Atmospheric Administration, Global Monitoring Laboratory (NOAA/GML), https://gml.noaa.gov/ccgg/trends/global.html, 2023.

Liu, J., Bowman, K., Lee, M., Henze, D., Bousserez, N., Brix, H., Collatz, G. J., Menemenlis, D., Ott, L., Pawson, S., Jones, D., and Nassar, R.: Carbon monitoring system flux estimation and attribution: impact of ACOS-GOSAT XCO_2XCO2 sampling on the inference of terrestrial biospheric sources and sinks, Tellus B, 66, 22486, https://doi.org/10.3402/tellusb.v66.22486, 2014.

Murphy, K. P.: Probabilistic Machine Learning: An Introduction, MIT Press, 864, ISBN 9780262046824, https://probml.github.io/pml-book/book1.html, 2022.

Nassar, R., Jones, D. B. A., Suntharalingam, P., Chen, J. M., Andres, R. J., Wecht, K. J., Yantosca, R. M., Kulawik, S. S., Bowman, K. W., Worden, J. R., Machida, T., and Matsueda, H.: Modeling global atmospheric CO2 with improved emission inventories and CO2 production from the oxidation of other carbon species, Geosci. Model Dev., 3, 689–716, https://doi.org/10.5194/gmd-3-689-2010, 2010.

Nathan, B. J., Lauvaux, T., Turnbull, J. C., Richardson, S. J., Miles, N. L., and Gurney, K. R.: Source Sector Attribution of CO2 Emissions Using an Urban CO CO2 Bayesian Inversion System, J. Geophys. Res.-Atmos., 123, 13611–13621, https://doi.org/10.1029/2018JD029231, 2018.

Noël, S., Buchwitz, M., Hilker, M., Reuter, M., Weimer, M., Bovensmann, H., Burrows, J. P., Bösch, H., and Lang, R.: Greenhouse gas retrievals for the CO2M mission using the FOCAL method: first performance estimates, Atmos. Meas. Tech., 17, 2317–2334, https://doi.org/10.5194/amt-17-2317-2024, 2024.

O'Dell, C. W., Connor, B., Bösch, H., O'Brien, D., Frankenberg, C., Castano, R., Christi, M., Eldering, D., Fisher, B., Gunson, M., McDuffie, J., Miller, C. E., Natraj, V., Oyafuso, F., Polonsky, I., Smyth, M., Taylor, T., Toon, G. C., Wennberg, P. O., and Wunch, D.: The ACOS CO2 retrieval algorithm – Part 1: Description and validation against synthetic observations, Atmos. Meas. Tech., 5, 99–121, https://doi.org/10.5194/amt-5-99-2012, 2012.

O'Dell, C. W., Eldering, A., Wennberg, P. O., Crisp, D., Gunson, M. R., Fisher, B., Frankenberg, C., Kiel, M., Lindqvist, H., Mandrake, L., Merrelli, A., Natraj, V., Nelson, R. R., Osterman, G. B., Payne, V. H., Taylor, T. E., Wunch, D., Drouin, B. J., Oyafuso, F., Chang, A., McDuffie, J., Smyth, M., Baker, D. F., Basu, S., Chevallier, F., Crowell, S. M. R., Feng, L., Palmer, P. I., Dubey, M., García, O. E., Griffith, D. W. T., Hase, F., Iraci, L. T., Kivi, R., Morino, I., Notholt, J., Ohyama, H., Petri, C., Roehl, C. M., Sha, M. K., Strong, K., Sussmann, R., Te, Y., Uchino, O., and Velazco, V. A.: Improved retrievals of carbon dioxide from Orbiting Carbon Observatory-2 with the version 8 ACOS algorithm, Atmos. Meas. Tech., 11, 6539–6576, https://doi.org/10.5194/amt-11-6539-2018, 2018.

Ohyama, H., Frey, M. M., Morino, I., Shiomi, K., Nishihashi, M., Miyauchi, T., Yamada, H., Saito, M., Wakasa, M., Blumenstock, T., and Hase, F.: Anthropogenic CO2 emission estimates in the Tokyo metropolitan area from ground-based CO_2 column observations, Atmos. Chem. Phys., 23, 15097–15119, https://doi.org/10.5194/acp-23-15097-2023, 2023.

Pandey, S., Houweling, S., Krol, M., Aben, I., Chevallier, F., Dlugokencky, E. J., Gatti, L. V., Gloor, E., Miller, J. B., Detmers, R., Machida, T., and Röckmann, T.: Inverse modeling of GOSAT-retrieved ratios of total column CH_4 and CO_2 for 2009 and 2010, Atmos. Chem. Phys., 16, 5043–5062, https://doi.org/10.5194/acp-16-5043-2016, 2016.

Peiro, H., Crowell, S., Schuh, A., Baker, D. F., O'Dell, C., Jacobson, A. R., Chevallier, F., Liu, J., Eldering, A., Crisp, D., Deng, F., Weir, B., Basu, S., Johnson, M. S., Philip, S., and Baker, I.: Four years of global carbon cycle observed from the Orbiting Carbon Observatory 2 (OCO-2) version 9 and in situ data and comparison to OCO-2 version 7, Atmos. Chem. Phys., 22, 1097–1130, https://doi.org/10.5194/acp-22-1097-2022, 2022.

Philip, S., Johnson, M. S., Potter, C., Genovesse, V., Baker, D. F., Haynes, K. D., Henze, D. K., Liu, J., and Poulter, B.: Prior biosphere model impact on global terrestrial CO2 fluxes estimated from OCO-2 retrievals, Atmos. Chem. Phys., 19, 13267–13287, https://doi.org/10.5194/acp-19-13267-2019, 2019.

Philip, S., Johnson, M. S., Baker, D. F., Basu, S., Tiwari, Y. K., Indira, N. K., Ramonet, M., and Poulter, B.: OCO-2 satellite-imposed constraints on terrestrial biospheric CO2 fluxes over South Asia, J. Geophys. Res.-Atmos., 127, e2021JD035035, https://doi.org/10.1029/2021JD035035, 2022.

Rodgers, C. D.: Inverse methods for atmospheric sounding: theory and practice, Atmospheric, Oceanic and Planetary Physics, edited by: World-Scientific, Singapore, London, 240 pp., 2000.

Roten, D., Lin, J. C., Das, S., and Kort, E. A.: Constraining Sector-Specific CO2 Fluxes Using Space-Based XCO_2XCO2 Observations Over the Los Angeles Basin, Geophysical Research Letters, 50, e2023GL104376. https://doi.org/10.1029/2023GL104376, 2023.

Safford, H. D., Paulson, A. K., Steel, Z. L., Young, D. J. N., and Wayman, R. B.: The 2020 California fire season: A year like no other, a return to the past or a harbinger of the future?, Global Ecol. Biogeogr., 31, 2005–2025, https://doi.org/10.1111/geb.13498, 2022.

Steel, Z. L., Jones, G. M., Collins, B. M., Green, R., Koltunov, A., Purcell, K. L., Sawyer, S. C., et al.: Mega-Disturbances Cause Rapid Decline of Mature Conifer Forest Habitat in California, Ecological Applications, https://doi.org/10.1002/eap.2763, 2022.

Turner, A. J., Kim, J., Fitzmaurice, H., Newman, C., Worthington, K., Chan, K., Wooldridge, P. J., Köehler, P., Frankenberg, C., and Cohen, R. C.: Observed impacts of covid-19 on urban CO_2 emissions, Geophys. Res. Lett., 47, e2020GL090037, https://doi.org/10.1029/2020GL090037, 2020.

United States Environmental Protection Agency: Inventory of U.S. Greenhouse Gas Emissions and Sinks, https://www.epa.gov/ghgemissions/inventory-us-greenhouse-gas-emissions-and-sinks (last access: December 21, 2023), 2023.

van Wees, D., van der Werf, G. R., Randerson, J. T., Rogers, B. M., Chen, Y., Veraverbeke, S., Giglio, L., and Morton, D. C.: Global biomass burning fuel consumption and emissions at 500 m spatial resolution based on the Global Fire Emissions Database (GFED), Geosci. Model Dev., 15, 8411–8437, https://doi.org/10.5194/gmd-15-8411-2022, 2022.

Vehtari, A., Gelman, A., and Gabry, J.: Practical Bayesian model evaluation using leave-one-out cross-validation and WAIC, Stat Comput,, 27, 1413–1432, https://doi.org/10.1007/s11222-016-9696-4, 2017.

Vermote, E. F. and Kotchenova, S.: Atmospheric correction for the monitoring of land surfaces, J. Geophys. Res., 113, D23S90, doi:10.1029/2007JD009662, 2008.

Wang, J.: An Intuitive Tutorial to Gaussian Processes Regression, arXiv, arXiv:2009.10862, 2023.

Williams, C. K. and Rasmussen, C. E.: Gaussian processes for machine learning, in: vol. 2, MIT Press, Cambridge, MA, 2006.

Wu, D., Lin, J., Oda, T., and Kort, E.: Space-based quantification of per capita CO2 emissions from cities, Environ. Res. Lett., 15, 035004, https://doi.org/10.1088/1748-9326/ab68eb, 2020.

857 Wu, D., Lin, J. C., Duarte, H. F., Yadav, V., Parazoo, N. C., Oda, T., and Kort, E. A.: A model for urban biogenic
858   CO2 fluxes: Solar-Induced Fluorescence for Modeling Urban biogenic Fluxes (SMUrF v1), Geosci. Model Dev.,
859   14, 3633–3661, https://doi.org/10.5194/gmd-14-3633-2021, 2021.

860 Wu, D., Liu, J., Wennberg, P. O., Palmer, P. I., Nelson, R. R., Kiel, M., and Eldering, A.: Towards sector-based
861   attribution using intra-city variations in satellite-based emission ratios between CO2 and CO, Atmos. Chem.
862   Phys., 22, 14547–14570, https://doi.org/10.5194/acp-22-14547-2022, 2022.

863 Yañez, C. C., Hopkins, F. M., Xu, X., Tavares, J. F., Welch, A., and Czimczik, C. I.: Reductions in California's urban
864   fossil fuel CO$_2$ emissions during the COVID-19 pandemic, AGU Advances, 3, e2022AV000732.
865   https://doi.org/10.1029/2022AV000732, 2022.

866 Yang, D. X., Liu, Y., Feng, L., Wang, J., Yao, L., Cai, Z. N., Zhu, S. H., Lu, N. M., and Lyu, D. R.: The First Global
867   Carbon Dioxide Flux Map Derived from TanSat Measurements, Adv. Atmos. Sci., 38, 1433–1443, 2021

868 Ye, X., Lauvaux, T., Kort, E. A., Oda, T., Feng, S., Lin, J. C., Yang, E. G., and Wu, D.: Constraining Fossil Fuel CO2
869   Emissions From Urban Area Using OCO-2 Observations of Total Column CO2, J. Geophys. Res.-Atmos., 125,
870   e2019JD030528, https://doi.org/10.1029/2019JD030528, 2020.

871